JM PAPERS

On the structure and dynamics of secondary flows over multicolumn roughness in channel flow

Atharva Sunil Sathe[1] , William Anderson[2] , Marc Calaf[3] and Marco Giometto[1]

[1]Department of Civil Engineering and Engineering Mechanics, Columbia University, New York, NY 10027, USA

[2]Department of Mechanical Engineering, The University of Texas at Dallas, 800 West Campbell Road, Richardson, TX 75080, USA

[3]Department of Mechanical Engineering, University of Utah, Salt Lake City, UT 84112, USA

Corresponding author: Marco Giometto, mg3929@columbia.edu

Secondary flows induced by spanwise heterogeneous surface roughness play a crucial role in determining engineering-relevant metrics such as surface drag, convective heat transfer and the transport of airborne scalars. While much of the existing literature has focused on idealized configurations with regularly spaced roughness elements, real-world surfaces often feature irregularities, clustering and topographic complexity for which the secondary flow response remains poorly understood. Motivated by this gap, we investigate multicolumn roughness configurations that serve as a regularized analogue of roughness clustering. Using large-eddy simulations, we systematically examine secondary flows across a controlled set of configurations in which cluster density and local arrangement are varied in an idealized manner, and observe that these variations give rise to distinct secondary flow polarities. Through a focused parameter study, we identify the spanwise gap between the edge-most roughness elements of adjacent columns, normalized by the channel half-height (s_a/H), as a key geometric factor governing this polarity. In addition to analysing the time-averaged structure, we investigate how variations in polarity affect the instantaneous dynamics of secondary flows. Here, we find that the regions of high- and low-momentum fluid created by the secondary flows alternate in a chaotic, non-periodic manner over time. Further analysis of the vertical velocity signal shows that variability in vertical momentum transport is a persistent and intrinsic feature of secondary flow dynamics. Taken together, these findings provide a comprehensive picture of how

the geometric arrangement of roughness elements governs both the mean structure and temporal behaviour of secondary flows.

Key words: boundary layer structure, atmospheric flows

1. Introduction

Understanding the dynamics of turbulent boundary layers is a long-standing challenge in fluid mechanics, with foundational studies dating back a hundred years (Prandtl 1925; Nikuradse 1933; Colebrook *et al.* 1937; Schlichting 1937). Turbulent boundary layers occur over various surfaces, including urban environments (Oke 1982; Oke *et al.* 2017; Meili *et al.* 2020), wind farms arrays (Calaf, Meneveau & Meyers 2010; Meyers & Meneveau 2013; Cortina *et al.* 2020), ships (Grigson 1992; Schultz 2000) and turbomachinery (Acharya *et al.* 1986) to name a few. When these rough surfaces exhibit spanwise heterogeneity comparable to the boundary layer height, they give rise to roughness-induced secondary flows. Unlike secondary flows of the first kind, which arise from vortex stretching and tilting mechanisms typically induced by curvature or rotation in the mean flow, these are the secondary flows of the second kind which arise from gradients in Reynolds stresses and are maintained through anisotropic turbulent production and dissipation (Hinze 1967; Anderson *et al.* 2015*a*). These secondary flows, characterized by streamwise vortical structures that redistribute momentum and energy in the spanwise-wall-normal plane, can significantly modify the mean flow field, alter turbulence intensities and influence quantities of engineering relevance such as surface drag and convective heat transfer.

Over the past decade, substantial research efforts have been devoted to advancing our understanding of secondary flows induced by surface roughness heterogeneities. Numerous experimental investigations (Barros & Christensen 2014; Vanderwel & Ganapathisubramani 2015; Kevin *et al.* 2017; Medjnoun, Vanderwel & Ganapathisubramani 2020; Wangsawijaya *et al.* 2020; Womack *et al.* 2022) and numerical studies (Willingham *et al.* 2014; Anderson *et al.* 2015*a*; Hwang & Lee 2018; Yang & Anderson 2018; Stroh *et al.* 2020; Joshi & Anderson 2022; Kaminaris *et al.* 2023; Sathe & Giometto 2024) have demonstrated the prevalence and significance of these flows across various roughness configurations. Typically, these secondary flows manifest as pairs of counter-rotating vortical structures whose dimensions scale with the characteristic spanwise spacing of the roughness elements. A distinctive hallmark of these secondary motions is the spanwise undulation of the mean streamwise velocity throughout the flow depth, resulting in clearly delineated low-momentum pathways (LMPs) and high-momentum pathways (HMPs) (Barros & Christensen 2014). Specifically, LMPs are bounded by vortical pairs oriented such that these pathways align with regions exhibiting upward vertical velocities. In contrast, HMPs align with regions of downward vertical velocities. These alternating momentum pathways recur periodically along the spanwise direction, directly reflecting the periodic arrangement of the roughness heterogeneity.

The self-sustaining nature of roughness-induced secondary flows is fundamentally tied to spanwise heterogeneities in the Reynolds stress components, which actively generate and maintain streamwise vorticity through turbulence anisotropy and vorticity production mechanisms (Anderson *et al.* 2015*a*). Gradients in both Reynolds normal and shear stresses arise due to spatial variations in surface roughness, which modulate the local turbulence intensity and stress distributions across the span. An alternative

yet complementary explanation for the maintenance of these secondary motions was proposed by Hinze (1967), based on the energy budget of turbulent kinetic energy (TKE). Assuming streamwise homogeneity and negligible transport contributions – assumptions valid for strip-type roughness configurations – the TKE budget reduces to a balance between production, dissipation and advection. In this framework, local imbalances between production ($\mathcal{P}$) and dissipation (ϵ) necessitate advection of TKE in the spanwise-wall-normal plane. Regions of excess production draw in turbulence-deficient fluid from the outer layer, inducing a downdraught above high-production zones. This fluid, having acquired elevated turbulence levels due to intense local shear and Reynolds stress production, becomes turbulence-rich and is laterally transported towards regions dominated by dissipation, generating spanwise outflow near the wall. The resulting turbulence-deficient fluid is advected upward, closing the circulation and giving rise to spanwise-periodic roll cells with distinct zones of updraught and downdraught. This cyclic redistribution of turbulence and momentum establishes that secondary flows are sustained by the spanwise modulation of $\mathcal{P} - \epsilon$ imposed by the underlying surface heterogeneity.

Analysis of flow over spanwise heterogeneous strip-type roughness has revealed that regions of elevated turbulent production coincide with areas of high roughness, whereas regions of excess dissipation align with low-roughness regions (Anderson *et al.* 2015a). This spatial disparity in the turbulence budget gives rise to secondary circulations in which LMPs and their associated updraughts emerge over low-roughness regions, while HMPs and corresponding downdraughts align with high-roughness areas. A similar alignment was reported in the experimental study of Barros & Christensen (2014), where flow over a turbine blade – damaged by the deposition of foreign material – exhibited LMPs over recessed roughness and HMPs over elevated deposits. In contrast, Vanderwel & Ganapathisubramani (2015), in their experiments involving streamwise-aligned Lego blocks (from the Danish phrase '*leg godt*' meaning 'play well') with varying spanwise spacing (commonly termed 'ridge-type' roughness), observed the opposite: LMPs were found over the elevated roughness, while HMPs occupied the recessed regions. This reversal in the alignment of secondary flow features – often referred to as flow polarity – has been a subject of ongoing debate ever since.

Direct numerical simulations (DNS) by Hwang & Lee (2018) of spatially developing turbulent boundary layer over smooth ridges also showed LMPs aligned with high roughness and HMPs with low roughness. In their analysis of the TKE budget equation, they uncovered that, similar to strip-type roughness, the production values exceed the dissipation value over the ridges. While their analysis of the TKE budget showed $\mathcal{P} - \epsilon > 0$ over the ridges, consistent with earlier findings from strip-type roughness, they found that the transport term (T) in the energy equation plays a critical role for ridge-type geometries and cannot be neglected. When included, the transport term reverses the net imbalance, such that $\mathcal{P} - \epsilon - T < 0$, implying that an upward advection of TKE is necessary over the ridges – thereby flipping the polarity of the secondary flows compared with the strip-type roughness. These findings firmly establish that either LMPs or HMPs (and their associated vertical motions) can align with the regions of high or elevated roughness, and that the polarity is dictated by the specific arrangement and geometry of the roughness elements.

Following the emergence of conflicting observations regarding the alignment of secondary flow structures with regions of high roughness, identifying the rough-surface parameters that influence flow polarity has become a central topic in the secondary flow community. Yang & Anderson (2018) investigated flow over streamwise-aligned rows of pyramidal obstacles and found that the lateral spacing between roughness features, s_y, when normalized by the boundary layer height H, acts as a governing

roughness parameter. Their results showed that for $s_y/H \lesssim 1$, updraughts tend to prevail over the pyramids – suggesting a flow polarity analogous to ridge-type roughness – while for $s_y/H \gtrsim 1$, domain-scale mean circulations emerged, with downdraughts aligning over the roughness rows-suggesting a flow polarity analogous to strip-type roughness. Building on the broader effort to characterize polarity-controlling parameters, Stroh *et al.* (2020) conducted DNS of flow over streamwise-aligned roughness strips and identified the relative elevation between smooth and rough regions as a key determinant of secondary flow polarity. When the smooth surface was recessed below the rough elements, updraughts formed over the high-roughness zones. However, raising the smooth surface to twice the roughness height reversed the polarity, with downdraughts now appearing over the rough strips. An intermediate state was observed when the smooth and rough surfaces were at the same height. Their analysis linked these changes in secondary-flow polarity to wall-normal deflections of spanwise velocity fluctuations, reflected in the sign change of the spanwise–wall-normal Reynolds stress component. Further contributions from Joshi & Anderson (2022), based on large-eddy simulations (LES) of flow over streamwise-aligned rows of synthetic trees, emphasized the importance of streamwise spacing between roughness elements. As the configuration transitioned from d-type to k-type roughness with increasing streamwise gap, they observed a corresponding reversal in secondary flow polarity – from updraughts over roughness rows (d-type) to downdraughts over them (k-type). Collectively, these studies establish that lateral spacing of spanwise heterogeneities, relative surface elevations and streamwise roughness spacing are critical parameters in determining secondary flow polarity for a given roughness configuration.

Another layer of complexity in understanding secondary flows lies in their temporal behaviour. While long-time-averaged fields often depict coherent, domain-scale counter-rotating vortices, recent studies have revealed that these structures are, in fact, the statistical imprint of smaller, intermittent and dynamically evolving motions. Kevin *et al.* (2017) investigated flow over a converging–diverging riblet pattern and demonstrated that the instantaneous secondary motions are composed of strong, compact vortices, far more intense than the large-scale structures observed in the mean flow. Their conditional averaging revealed that only 28 % of the snapshots bore resemblance to the pair of counter-rotating vortices seen in long-time-averaged fields. Interestingly, in 31 % of the cases, the flow exhibited large-scale, one-sided rotational motions, which occurred more frequently than symmetric vortex pairs. The remaining 41 % of the snapshots showed no resemblance to the time-averaged secondary flow structures. This lead to the conclusion that the domain-scale secondary flows are artefacts of time-averaging, obscuring a highly transient flow field beneath. This view was refined by Vanderwel *et al.* (2019), who, through a combination of experiments and DNS over ridge-type roughness, revealed that the large-scale secondary flows observed in the time-averaged fields are the ensemble imprint of numerous compact, counter-rotating vortex pairs appearing in the instantaneous flow. These structures, smaller in size yet significantly stronger than the mean vortices, occur in varying orientations and are distributed asymmetrically across the span. Their findings emphasized that the apparent coherence of secondary flows in the mean arises from a non-homogeneous spatial distribution of these transient vortical events, rather than from persistent, rigid roll structures. Additionally, Anderson (2019) modelled the secondary flow system using a reduced-order dynamical framework and demonstrated the potential for spontaneous polarity reversals, indicating chaotic, non-periodic behaviour in the evolution of these flows akin to chaotic attractors. Additional insights into the temporal dynamics of secondary flows were provided by Wangsawijaya *et al.* (2020), who showed that the secondary flows meander and shift in response to spanwise heterogeneity, with time-dependence most pronounced when the roughness wavelength matches the boundary
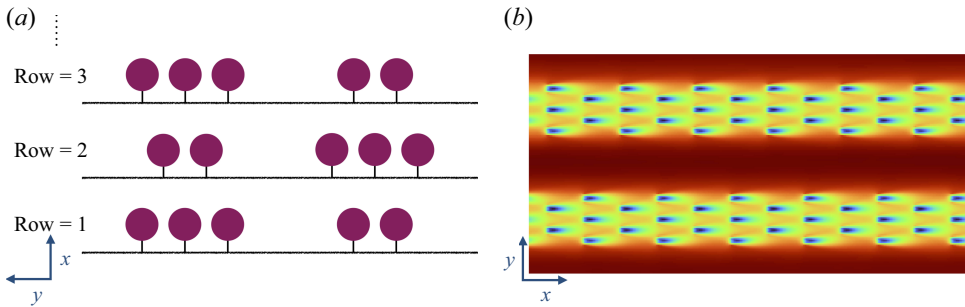
Figure 1. (*a*) Schematic of roughness element arrangement (not to scale; flow direction is bottom to top) and (*b*) mean streamwise velocity at mid-element height (flow direction is left to right) for S2-5-2 case.

layer thickness ($s_y/H \approx 1$). Similar to the aforementioned studies, their results emphasized that the apparent coherence of secondary flows may be a manifestation of averaging over time-dependent, spatially localized motions. Collectively, these studies indicate that secondary flows are not steady-state features but evolve through a complex interplay of intermittent vortices, unsteady momentum pathways and potentially chaotic dynamics, all of which must be considered for a complete understanding of their behaviour.

Recently, Womack *et al.* (2022) reported the existence of secondary flows over a surface populated with irregularly arranged truncated cones, despite the absence of any regularized spanwise heterogeneity in the roughness layout. They hypothesized that these secondary motions originate near the leading edges of the roughness topography and can persist over extended streamwise distances, even as the downstream topography varies significantly. This hypothesis was subsequently examined and supported through detailed DNS investigations by Kaminaris *et al.* (2023). However, in their analysis, the roughness configurations were deliberately designed to eliminate clustering and directional bias, focusing instead on more homogeneously distributed roughness. While the study of such surfaces is certainly relevant, clustering and directional bias are also common features in many real-world environments. Examples include the patchy deposition of foreign materials on turbine blades (Barros & Christensen 2014), marine biofouling on ship hulls and offshore structures (Schultz 2007), random ice accretion on aircraft surfaces (Bragg, Broeren & Blumenthal 2005) and atmospheric boundary layers over complex terrain (Giometto *et al.* 2016). This raises an important question: How might the presence of roughness clustering, where multiple closely spaced elements collectively act as a high-drag region, influence the structure and dynamics of secondary flows? To date, most studies have focused on canonical configurations where each streamwise-aligned high-drag zone typically corresponds to a single roughness element in the spanwise direction (Vanderwel & Ganapathisubramani 2015; Hwang & Lee 2018; Yang & Anderson 2018; Joshi & Anderson 2022; Sathe & Giometto 2024). Given the critical role the secondary flows play in determining engineering-relevant metrics such as surface drag, heat transfer and momentum redistribution, it is essential to understand how parameters such as cluster density and local topography influence these resulting circulations.

To advance this understanding, we investigate a multicolumn roughness configuration, visualized in figure 1, that serves as a regularized analogue of roughness clustering. This set-up allows for precise control of geometric parameters, enabling systematic exploration of secondary flow polarity. The configuration consists of multiple resolved roughness elements combined in both the streamwise and spanwise directions to form well-defined, streamwise-aligned high-roughness regions. Here, individual roughness

elements are modelled as momentum-absorbing obstacles resembling wind turbines, providing a simplified representation of flow through porous media (Calaf *et al.* 2010). We vary cluster density by systematically adjusting the lateral spacing between roughness elements within each column, while maintaining a constant streamwise gap across all cases. In addition, we examine the impact of local arrangement by comparing staggered and aligned configurations within the multicolumn set-up. Overall, this study aims to advance our understanding of how roughness clustering influences secondary flow behaviour by examining both time-averaged and instantaneous flow characteristics within this controlled, yet physically relevant framework.

The paper is organized as follows. Section 2 outlines the methodology employed in this study, including the simulation algorithm (§ 2.1) and the simulation set-up, along with the naming conventions used to describe the various configurations (§ 2.2). The characteristics of the time-averaged secondary flows are examined in § 3, where we identify a key parameter that governs the polarity of secondary flows in the multicolumn roughness configuration. Section 4 explores the temporal dynamics of secondary flows with differing polarities, providing insight into their unsteady behaviour. Finally, § 5 provides the conclusions drawn from the study.

2. Methodology

2.1. *Simulation algorithm*

A suite of LES of flow over windfarm arrays is performed in this study using an in-house code (Albertson & Parlange 1999*a*,*b*; Bou-Zeid, Meneveau & Parlange 2005; Chamecki, Meneveau & Parlange 2009; Calaf *et al.* 2010; Meyers & Meneveau 2013; Anderson *et al.* 2015*b*; Fang & Porté-Agel 2015; Giometto *et al.* 2016; Li *et al.* 2016; Sharma *et al.* 2016; Cortina *et al.* 2020; Hora & Giometto 2024; Li & Giometto 2024). The filtered Navier–Stokes equations are solved in their rotational form (Orszag & Pao 1975) to ensure the conservation of mass and kinetic energy in the inviscid limit, i.e.

$$\frac{\partial \tilde{u}_i}{\partial x_i} = 0 \,, \tag{2.1}$$

$$\frac{\partial \tilde{u}_i}{\partial t} + \tilde{u}_j \left(\frac{\partial \tilde{u}_i}{\partial x_j} - \frac{\partial \tilde{u}_j}{\partial x_i} \right) = -\frac{1}{\rho} \frac{\partial \tilde{p}^*}{\partial x_i} - \frac{\partial \tau_{ij}^{SGS}}{\partial x_j} - \frac{1}{\rho} \frac{\partial \tilde{p}_\infty}{\partial x_1} \delta_{i1} + \tilde{F}_i \,, \tag{2.2}$$

where $\tilde{u}_1$, $\tilde{u}_2$ and $\tilde{u}_3$ are the filtered velocities along the streamwise x_1, spanwise x_2 and wall-normal x_3 directions, respectively, and ρ is the reference density. In this study, index notation is used for compact representation of governing equations, while the more conventional meteorological notation – where u, v and w denote the velocities in streamwise (x), spanwise (y) and vertical (z) directions, respectively – is used in the discussions. The deviatoric component of the subgrid-scale (SGS) stress tensor (τ_{ij}^{SGS}) is evaluated via the Lagrangian scale-dependent dynamic Smagorinsky model (Bou-Zeid *et al.* 2005). The Lagrangian scale-dependent dynamic model has undergone rigorous validation in a range of turbulent flow scenarios, including wall-modelled LES of the atmospheric boundary layer (Momen & Bou-Zeid 2017; Salesky, Chamecki & Bou-Zeid 2017), as well as in complex flows over urban-like surfaces and canopy geometries (Anderson *et al.* 2015*b*; Giometto *et al.* 2016; Li *et al.* 2016; Yang 2016; Li & Giometto 2023; Sathe & Giometto 2024). Given the high Reynolds number regime considered, viscous stresses are omitted and wall stress is instead computed using an inviscid logarithmic law of the wall appropriate for fully rough surfaces

(Giometto *et al.* 2016). Neglecting viscous stresses is valid under the assumption that SGS stress contributions are predominantly from the pressure field. To incorporate SGS pressure effects and resolved kinetic energy, the pressure field is redefined using a modified form: $\tilde{p}^* = \tilde{p} + (1/3)\rho\tau_{ii}^{SGS} + (1/2)\rho\tilde{u}_i\tilde{u}_i$. The flow is driven by a spatially uniform pressure gradient. The magnitude of friction velocity u_τ is linked to this pressure gradient through the relation $(-\nabla p/\rho)H = u_\tau^2$, where H is the half-channel height. This allows the friction velocity to be an input parameter for this study. Periodic boundary conditions are imposed in the streamwise and spanwise directions, while the upper boundary has a free-slip boundary condition, satisfying $w = 0$, $\partial u/\partial z = 0$ and $\partial v/\partial z = 0$. The lower surface consists of arrays of wind turbines, where the standard actuator disk model without rotation is used to parameterize the turbine induced forces ($\tilde{F}_i$) (Jimenez *et al.* 2007; Calaf *et al.* 2010; Wu & Porté-Agel 2011). Based on the scope of this study, the actuator disk model with rotation is not introduced as the model without rotation can accurately capture first- and second-order statistics in the far-wake region (Wu & Porté-Agel 2011) as well as the mean kinetic energy pathways (Meyers & Meneveau 2013). It is important to note that this is not a wind-energy study; rather, wind turbines are used here as representative porous roughness elements commonly found in both built and natural environments.

The spatial derivatives in the wall-parallel directions are performed using a pseudospectral collocation method that relies on truncated Fourier expansions (Orszag 1970). In contrast, discretization in the vertical direction employs a second-order accurate finite-difference scheme on a staggered grid. Time advancement is carried out using an explicit second-order Adams–Bashforth scheme. To accurately handle the nonlinear advection terms and prevent aliasing errors, a 3/2 padding rule is applied (Canuto *et al.* 2007; Margairaz *et al.* 2018). The incompressibility constraint, expressed in (2.1), is enforced through a fractional-step method (Kim & Moin 1985). The simulations are averaged for $120T$, where T is the large eddy turnover time defined as $T = H/u_\tau$ to ensure temporal convergence of first- and second-order statistics. This averaging period is approximately $7\times$ larger than what is typically used in simulations of flow over obstacles (Coceal *et al.* 2006; Claus *et al.* 2012; Tian, Conan & Calmet 2021). The time step employed in these simulations is selected to maintain a Courant–Friedrichs–Lewy number below 0.1, ensuring numerical stability.

2.2. *Simulation set-up and naming convention*

Different roughness element arrangements are explored in this study to analyse the secondary flow response in a multicolumn set-up. The size of the computational domain is $[0, L_x] \times [0, L_y] \times [0, H]$, where $L_x/H = 6$, $L_y/H = 3$ and $H/h = 12$, where h represents the elevation of the actuator disk centre. The scale separation and aspect ratio of the domain is chosen based on extensive analysis provided in Sathe & Giometto (2024), where the impact of the numerical domain on turbulent flow statistics is examined for canopy flows. Diameter of the disks (D) is kept constant $D/h = 1$ for all the simulations. An aerodynamic roughness length of $z_0 = 10^{-6}h$ is prescribed at the lower surface via the wall-layer model. With the chosen value of z_0, the SGS pressure drag is a negligible contributor to the overall momentum balance (Yang & Meneveau 2016). The flow is in fully rough aerodynamic regime with a roughness Reynolds number $Re_\tau \equiv u_\tau h/\nu = 4.5 \times 10^6$. The domain is discretized using a uniform Cartesian grid of $N_x \times N_y \times N_z = 576 \times 288 \times 192$. This resolution ensures eight grid points per diameter in the spanwise direction and 16 grid points per diameter in the vertical direction, which is shown to be adequate to accurately capture first- and second-order flow statistics (Wu & Porté-Agel 2011).

The cases considered in this study consist of various configurations of roughness elements which are named as detailed in (2.3). Schematic and flow field visualization is shown for a sample case S2-5-2 in figure 1. In this naming convention, the first symbol indicates whether the elements within each column are locally staggered (denoted by 'S') or aligned (denoted by 'A'). The second symbol represents the spanwise gap between elements within the same column, normalized by the diameter. The third symbol corresponds to the total number of elements per row. As illustrated in figure 1(*a*), the locally staggered configuration also involves a streamwise staggering to maintain an equal number of elements per row. The fourth symbol indicates the total number of wider columns, each of which may contain multiple elements in the spanwise direction. The centres of these wider columns are uniformly spaced across the spanwise extent of the domain. To elaborate, the case S2-5-2, which is depicted in figure 1, denotes a locally staggered arrangement (S), where the spanwise gap between the centres of elements in the same wider column is twice the element diameter (S2). This configuration includes five elements per row (S2-5), which are distributed in two wider columns (S2-5-2).

$$ \text{Case} \equiv \underbrace{(\text{Symbol 1})}_{\substack{\text{Element} \\ \text{configuration}}} \quad \underbrace{(\text{Symbol 2})}_{\substack{\text{Spanwise gap} \\ \text{between elements} \\ \text{of the same column}}} - \underbrace{(\text{Symbol 3})}_{\substack{\text{Total number} \\ \text{of elements} \\ \text{per row}}} - \underbrace{(\text{Symbol 4})}_{\substack{\text{Number of} \\ \text{larger} \\ \text{columns}}} . \quad (2.3) $$

3. Time averaged secondary flows and their characteristics

This section investigates the influence of various parameters in a multicolumn roughness configuration on the polarity of secondary flows. Initially, four cases are examined in § 3.1, where two cases exhibit a reversal in polarity, while the other two represent an intermediate state. Based on an analysis of mean kinetic energy pathways, a hypothesis is formulated which identifies the critical parameter governing polarity. In subsequent subsections, other parameters are systematically ruled out as critical, thereby reinforcing the proposed hypothesis.

The operation of time-averaging is denoted by $\overline{(\cdot)}$, while the angled brackets $\langle \cdot \rangle$ denote horizontal averaging operation, with the subscripts indicating the direction of averaging. Deviations from the time-averaged quantities are denoted by $(\cdot)'$, and the deviations from both the space and time-averaged quantities are denoted by $(\cdot)''$ (Raupach & Shaw 1982; Schmid *et al.* 2019). It is important to note that all second-order statistics discussed are computed using the resolved portion of the flow field, as the contributions from the SGS components are observed to be negligible.

3.1. *Identifying the critical parameter governing secondary flow polarity*

In this subsection, we aim to study parameters in the multicolumn roughness configuration that govern the polarity of secondary flows. The roughness element arrangement considered involves multiple length scales of interest, as shown in figure 2. Here, the length scale s_l refers to the local spanwise gap between adjacent elements of the same wider column, while s_a refers to the spanwise gap between adjacent elements of the neighbouring wider columns. Since the elements are staggered in the streamwise direction as shown in figure 1(*a*), s_a remains constant across all rows. The length scale s_w refers to the total width of a column, defined as the maximum spanwise gap between elements within the same column. Although the left-hand column appears wider than the right-hand column in figure 2, s_w is identical for both columns due to staggered arrangement, which

Case	s_l/D	s_w/D	s_a/H	s_y/H	s_x/h	z_0/h	d/h	k_s/h
S2-5-2	2	4	1.25	1.5	4.5	0.016	0.163	0.406
S2.75-5-2	2.75	5.5	1.156	1.5	4.5	0.017	0.201	0.447
S3.5-5-2	3.5	7	1.063	1.5	4.5	0.023	0.060	0.594
S4-5-2	4	8	1	1.5	4.5	0.025	0.029	0.651

Table 1. Suite of simulations for secondary flow reversal in § 3.1. The naming scheme for cases is defined in (2.3) and length scales (s_l, s_w, s_a and s_y) are shown in figure 2. Here s_x is the streamwise gap between the element rows.
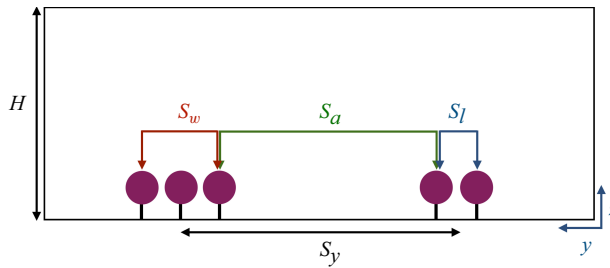
Figure 2. Schematic of length scales considered in the roughness element arrangement. Here s_l, spanwise gap between adjacent elements of the same wider column; s_w, width of the wider column; s_a, spanwise gap between adjacent elements of different wider columns; s_y, spanwise gap between centres of different wider columns.

can be appreciated from the mean flow field visualized in figure 1(*b*). The length scale s_y refers to the spanwise distance between the centres of the wider columns, while H is the height of the half-channel. In this paper, the lateral length scales confined to a single wider column (s_l and s_w) are normalized with D, while the length scales corresponding to different wider columns (s_a and s_y) are normalized with H. The streamwise spacing between element rows, denoted by s_x, is normalized by h.

Based on variations in these length scales, four different arrangements of roughness elements are obtained which are outlined in table 1. The case names reflect changes in only the second symbol, which corresponds to the length scale s_l/D. As shown in the table, altering s_l/D also affects parameters s_w/D and s_a/H, due to their inherent interdependence. Since s_y/H and s_x/h have previously been identified as critical parameters influencing the polarity of secondary flows (Yang & Anderson 2018; Joshi & Anderson 2022), they are fixed at a constant value across all four cases to eliminate their influence from the current analysis.

Figure 3 presents the horizontally averaged first- and second-order statistics for the four configurations listed in table 1. In rough-wall flows, the mean streamwise velocity profile in the logarithmic region is often characterized using the aerodynamic roughness length z_0 and the displacement height d, as

$$\frac{\langle \overline{u} \rangle}{u_\tau} = \frac{1}{\kappa} \ln \left(\frac{z - d}{z_0} \right), \tag{3.1}$$

where $\kappa = 0.384$ is the von Kármán constant used in this study. Owing to the pronounced spanwise heterogeneities introduced by secondary flows, as will be demonstrated later through flow visualizations, prior studies have shown that horizontally averaged profiles in such flows generally deviate from the classical log-law scaling (Castro *et al.* 2021; Sathe & Giometto 2024). Surprisingly, however, all four cases examined here exhibit
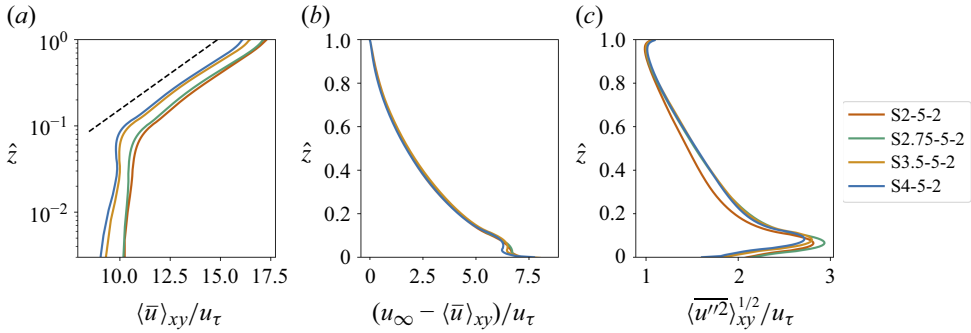
Figure 3. (*a*) Spatially averaged mean streamwise velocity, (*b*) velocity defect and (*c*) root mean squared velocity profiles for the cases considered in table 1. The black dashed line in (*a*) denotes the log-law slope. Here $\hat{z} = (z - d)/(H - d)$.
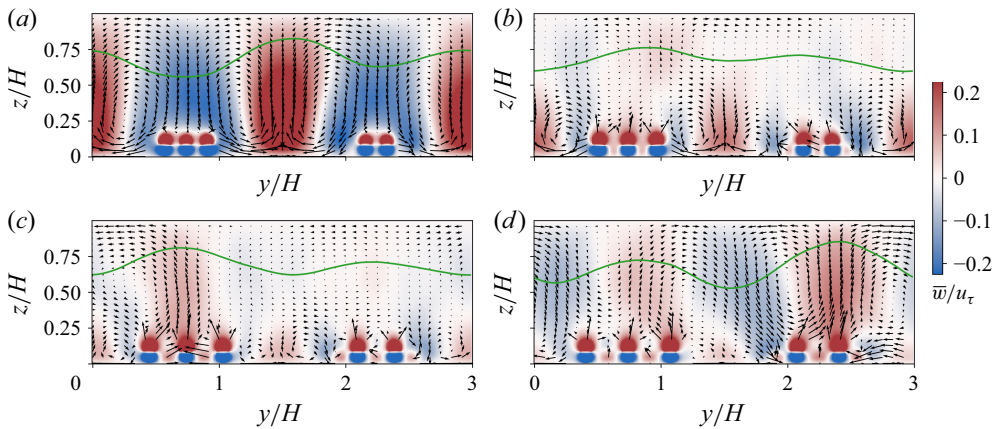

Figure 4. Pseudocolour plot of vertical velocity for different cases mentioned in table 1, taken at a streamwise location coinciding with the elements. Here (*a*) S2-5-2, (*b*) S2.75-5-2, (*c*) S3.5-5-2, (*d*) S4-5-2. The black arrows indicate the vectors of spanwise and vertical velocity. The green line indicates contour of 95 % of horizontally averaged maximum mean streamwise velocity.

a discernible logarithmic region, suggesting that the porous and elevated nature of the roughness elements helps preserve near-logarithmic scaling in the mean profile. The corresponding aerodynamic roughness lengths z_0 and displacement heights d are listed in table 1. For reference, the equivalent sand-grain roughness height, computed as $k_s = z_0 e^{8.5\kappa}$, is also reported in the same table (Womack *et al.* 2022). Furthermore, while the normalized velocity defect profiles collapse across all four cases, the total streamwise fluctuation profiles, comprising both temporal and dispersive contributions, exhibit a noticeable departure for case S2-5-2.

Figure 4 shows the pseudocolour plot of mean vertical velocity for these cases. The mean flow field is averaged over repeating patterns of roughness elements in the streamwise direction to improve symmetry. Since the structure of the mean secondary flows remains largely unchanged as the flow evolves within each repeating unit, we present only a representative $Y-Z$ slice taken at the streamwise location coinciding with the element rows. Here, the obstacles appear as distinct elements with their own local updraughts and downdraughts divided at the middle of the rotor disk. This is due to the non-rotational nature of the actuator disk model used in this study.

It can be clearly seen that as the local spanwise gap between the elements (s_l/D) is varied systematically, the response of the flow due to the roughness arrangement changes significantly. For the case S2-5-2, where elements are placed close to each other, half-channel height-scale secondary flows (here onwards referred to as delta-scale secondary flows) are distinctly seen. Such delta-scale secondary flows are also observed in numerical studies of flow over modelled roughness (Willingham *et al.* 2014; Anderson *et al.* 2015*a*; Chung, Monty & Hutchins 2018), resolved roughness of different types (Hwang & Lee 2018; Yang & Anderson 2018; Stroh *et al.* 2020) and in experimental studies (Vanderwel & Ganapathisubramani 2015; Kevin *et al.* 2017), when $s_y/H \gtrsim 1.5$. However, different polarity of these delta-scale secondary flows is also reported in these studies. In figure 4(*a*), clear downdraughts are seen over the elements for case S2-5-2. Consequently, strong updraughts are observed in the valley between the elements due to the secondary flows. As s_l/D is systematically increased, the flow response for cases S2.75-5-2 and S3.5-5-2 differs significantly. The delta-scale vortices disappear in the mean flow for these configurations, and as a consequence, no prominent updraughts or downdraughts are observed coinciding with both the element columns symmetrically. As s_l/D is further increased, the delta-scale secondary flows reappear, but this time, strong updraughts are seen over the elements for the case S4-5-2, accompanied by strong downdraughts in the valley. Observations of the vertical velocity at the domain centre show that the extent of the updraught in the valley, originating at the wall, decreases monotonically with increasing s_l/D. Figure 4 also includes the 95 % contour of the horizontally averaged maximum mean streamwise velocity, highlighting the spanwise variations in the mean streamwise flow. For the case S2-5-2, the contour shows significant modulation of mean streamwise velocity in a way such that the higher momentum fluid flows over the elements and the flow slows down significantly in the valley between the elements. Significant reduction in the modulation of mean streamwise velocity is observed for S2.75-5-2, whereas a reversed modulation starts appearing for S3.5-5-2, where the flow slows down over the elements and speeds up in the valley. This reversed modulation is strengthened for the case S4-5-2, where the LMPs align with the updraughts over the elements. This clearly showcases that as the parameter s_l/D is changed, the mean secondary rolls rearrange themselves to change the locations of LMPs and HMPs with respect to the roughness arrangement.

Figure 5 shows the TKE at Y–Z plane coinciding with the element row for the cases discussed above. For all the cases, maximum TKE lies in the vicinity of the roughness compared with the valley, regardless of the polarity of secondary flows. However, the way this TKE, generated near the roughness elements, is subsequently advected throughout the flow depends strongly on the polarity of the secondary circulation. For the case S2-5-2, due to strong downdraughts occurring over the element rows, the TKE generated by the elements is advected down and towards the valley. This can be appreciated by looking at the contour of 20 % of maximum TKE. Despite having two large sources in the spanwise direction that generate TKE, the 20 % contour does not show any significant hills or valleys for this case, indicating that the TKE is well-mixed in the spanwise direction. As s_l/D is increased, hills in the contour of TKE start appearing coinciding with the element rows. This is expected, as the secondary rolls rearrange themselves to favour updraughts over the elements, which results in the generated TKE by elements being advected upwards. This creates significant spanwise heterogeneity in the magnitude of TKE which is sustained deep in the outer layer.

While a reversal in secondary flow polarity is observed as s_l/D is changed, it does not necessarily imply that s_l/D is the critical parameter governing the polarity of secondary flows. From table 1, it is seen that changing s_l/D also changes parameters s_w/D and s_a/H due to their interdependence, and each of these parameters could be critical for
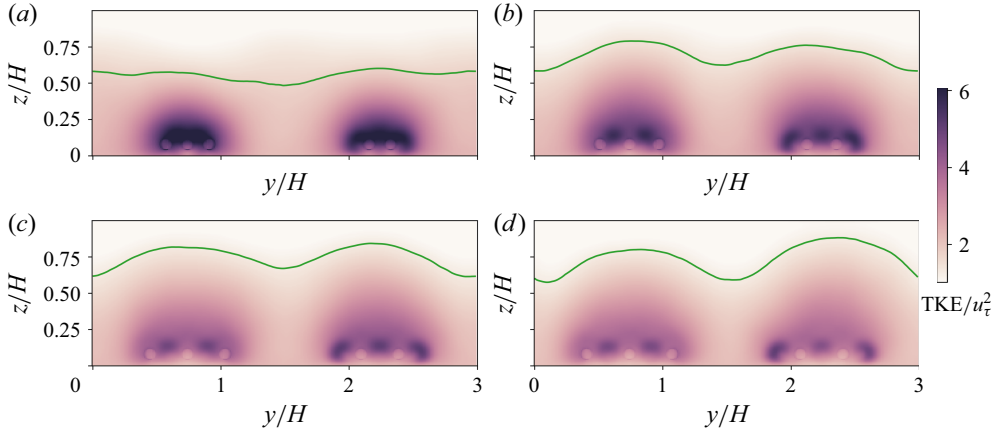
Figure 5. Pseudocolour plot of TKE for different cases mentioned in table 1, taken at a streamwise location coinciding with the elements. Here (*a*) S2-5-2, (*b*) S2.75-5-2, (*c*) S3.5-5-2, (*d*) S4-5-2. The green line indicates contour of 20 % of maximum TKE on the visualized plane.

the flow response observed in figure 4. Furthermore, these observations are made for a locally staggered arrangement, which was chosen so that the parameter s_l/D can be increased without the formation of local valleys within the same column. However, in a staggered arrangement, as in contrast with an aligned arrangement, shear emanating from the upstream element may freely impinge on the downstream element, which can have a critical impact on the value of production term in the TKE budget equation. As the imbalance between production, dissipation and transport terms in the TKE budget is shown to drive the secondary flow polarity (Hinze 1967; Anderson *et al.* 2015*a*; Hwang & Lee 2018; Joshi & Anderson 2022), it is unclear, thus far, whether the flow response observed is specific to the local staggered arrangement used in the study. Hence, further investigation is needed to accurately isolate these parameters and determine their effect on the secondary flow polarity. The subsequent analysis in this subsection only focuses on the cases S2-5-2 and S4-5-2 as they show clear reversal in secondary flow polarity. While the long-time-averaged flow fields for cases S2.75-5-2 and S3.5-5-2 may give the impression that delta-scale secondary flows are absent, this is not an accurate reflection of the instantaneous flow dynamics. In these cases, no single pathway remains dominant over time; instead, frequent switching between pathways leads to a weakening of the secondary flow signatures in the mean visualization. A detailed discussion of this behaviour is provided in § 4.

To investigate the parameter critical to the reversal in secondary flow polarity, we use the energy transport tubes introduced in Meyers & Meneveau (2013) to identify pathways taken by the kinetic energy of the mean flow (MKE) which is extracted by a given roughness element. Similar to the concept of classical mass transport tubes, energy transport tubes are defined such that no fluxes of energy exist over the tube mantle. The flux vector of MKE can be defined based on its transport equation,

$$\frac{\partial}{\partial x_j}\left(\overline{E}_j\right) = -\frac{1}{\rho}\frac{\partial \overline{u}_i \overline{p}_\infty}{\partial x_i} + \overline{u_i' u_j'}\frac{\partial \overline{u}_i}{\partial x_j} - 2\nu \overline{S}_{ij}\overline{S}_{ij} + \frac{1}{\rho}\overline{u}_i \overline{F}_i \,, \tag{3.2}$$

where

$$\overline{E}_j = \overline{K}\,\overline{u}_j + \left(\frac{\overline{p}}{\rho}\delta_{ij} + \overline{u_i' u_j'} - 2\nu \overline{S}_{ij}\right)\overline{u}_i, \tag{3.3}$$

Case	s_l/D	s_w/D	s_a/H	s_y/H	s_x/h
A0-3-3	N/A	N/A	1	1	4.5
A0-2-2	N/A	N/A	1.5	1.5	4.5

Table 2. Additional suite of simulations for energy tube evolution. The naming scheme is defined in (2.3). The length scales are the same as in table 1.

is the mean kinetic energy flux vector per unit mass, $\overline{K} = (\overline{u}_i \overline{u}_i / 2)$ is the MKE, $\overline{S}_{ij}$ is the mean strain rate tensor and $\overline{p}$ represents the part of pressure responsible for pressure gradient other than the externally applied pressure gradient ($\overline{p}_\infty$). Equation (3.3) shows that the energy transport tube differs from classical mass transport tube due to the pressure, turbulence and viscous transport terms. As the Reynolds number for all the cases under investigation is very high, the contribution of viscosity is neglected. From (3.2), it is evident that the right-hand side contains both sources and sinks of energy. Therefore, unlike mass transport tubes, the total energy within an energy transport tube may not be conserved (Meyers & Meneveau 2013).

Before analysing the mean energy transport tubes for cases S2-5-2 and S4-5-2, we first consider simpler aligned cases to understand the preferential pathways for MKE entrainment for the range of s_a/H and s_y/H values under investigation, which are detailed in table 1. Meyers & Meneveau (2013, see their figure 10) showcased variations in the shapes of energy tubes with varying s_y/D. In their investigation for aligned configuration, they considered different values of s_y/D, ranging from 4.54 to 10.5. They showcased that as s_y/D is progressively increased, the elements favour spanwise entrainment of MKE compared with the vertical entrainment. When normalized by the half-channel height, i.e. considering s_y/H instead of s_y/D, this parameter range corresponds to 0.454–1.05 for their study. However, it is well known that as s_y/H is increased further, delta-scale secondary flows appear and strong inhomogeneities in Reynolds stresses are observed associated with these secondary motions (Willingham *et al.* 2014; Vanderwel & Ganapathisubramani 2015; Yang & Anderson 2018). Thus, considering the contribution of advection and Reynolds stresses in (3.3), it is unclear whether the preferential spanwise entrainment of MKE with increasing s_y/H continues for $s_y/H > 1$. To investigate this, we run two cases with $s_y/H = 1$ and 1.5, as detailed in table 2. These cases have aligned configuration with only one element per column in the spanwise direction to mimic the cases considered in Meyers & Meneveau (2013). The streamwise gap between the elements is kept equal to the cases shown in table 1 to facilitate comparison with S2-5-2 and S4-5-2.

Figure 6 presents the pseudocolour plot of vertical velocity and modulation of mean streamwise velocity for these cases. For case A0-3-3, which corresponds to $s_y/H = 1$, weak downdraughts are observed over the elements and updraughts are observed in the valley. However, the effect of these circulations on the mean streamwise velocity is minimal. On the other hand, for the case A0-2-2, which corresponds to $s_y/H = 1.5$, strong delta-scale secondary flows are observed with HMPs and corresponding downdraughts coinciding with the elements. The effect of these circulations on the mean energy transport tubes is depicted in figure 7. For the case A0-3-3, the energy tube expands in both the vertical and the spanwise direction equally. We note that this shape differs from the case with $s_y/H = 1.05$ considered in Meyers & Meneveau (2013) due to the comparatively smaller streamwise gap considered in our study. For A0-3-3, initially, the growth rate is higher in the spanwise direction. However, as the upstream distance increases, the lower-half of the energy tube starts converging to a single line indicating diminishing spanwise
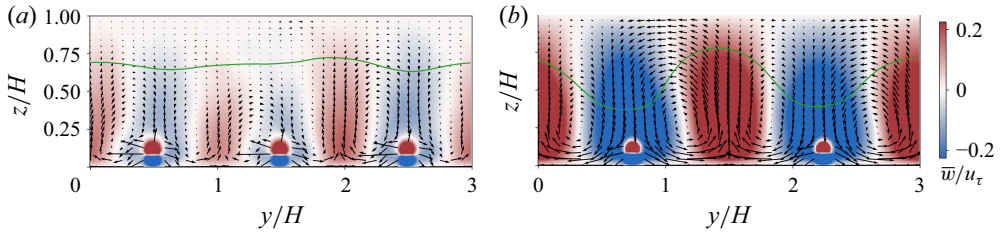
Figure 6. Pseudocolour plot of vertical velocity for different cases mentioned in table 2, taken at a streamwise location coinciding with the elements. Here (*a*) A0-3-3, (*b*) A0-2-2. The black arrows indicate the vectors of spanwise and vertical velocity. The green line indicates contour of 95 % of maximum mean streamwise velocity.

growth, whereas the vertical growth is still noticeable until $x = -34s_x D$. However, in contrast, the energy tube for A0-2-2 is noticeably narrower and taller. By analysing the maximum vertical and spanwise distance of the location of the MKE which is entrained by the elements, which is shown in figure 7(*b*,*d*), it is clear that the case A0-2-2 favours vertical entrainment of MKE over the spanwise entrainment compared with A0-3-3. This showcases that the observed trend of increasing spanwise entrainment with increasing s_y/H for $s_y/H \lesssim 1$ is reversed due to secondary circulations as s_y/H increases beyond unity. This is expected, as in this case, the secondary circulations align the higher-momentum fluid with the region above the elements, and strong downdraughts facilitate its downward transport. From this analysis, we can see that the shape and evolution of the mean energy transport tube encodes the information of polarity of secondary circulations. This is because as we move away from the elements, the contribution of pressure transport and turbulent transport in (3.3) decreases. Thus, the location of extremities of the tube far away from the elements indicates the direction of advection. Specifically, a narrower and taller tube indicates downdraught over the elements, which forms a circulation such that the flow is advected from the elements towards the valley (see, e.g. figure 4*a*). In contrast, a shorter and wider tube indicates spanwise advection of MKE, which forms a circulation such that the flow is advected from the valley towards the elements, which results in updraughts over the elements (see, e.g. figure 4*d*). For the cases such as A0-3-3 where the energy tube is equally wider and taller, formation of HMPs and LMPs is not observed which is reflected in weak modulation of mean streamwise velocity shown in figure 6(*a*). It should also be noted that, for both A0-3-3 and A0-2-2, the two parameters s_a/H and s_y/H are identical. Thus, this change in entrainment pathway of MKE with changing s_y/H can also be interpreted as a change due to changing s_a/H, which denotes the gap between adjacent elements in the spanwise direction.

Figure 8 shows the mean energy transport tubes for cases S2-5-2 and S4-5-2 along with the maximum vertical and spanwise distance at which the MKE is entrained by the elements. To enable direct comparison, the two layouts are overlaid, and we focus on the column segment containing three elements, where the central elements coincide and the edge elements are offset according to their respective s_l/D values. To maintain visual clarity, the transport tubes associated with the central element are omitted, as the focus here is on the entrainment behaviour of the edge elements. The figure shows a clear contrast in the entrainment mechanisms between the two cases. In case S2-5-2, the elements predominantly entrain MKE from above, indicating a vertically dominant entrainment pathway. In contrast, case S4-5-2 exhibits stronger spanwise entrainment. Interestingly, this shift in entrainment direction occurs despite both configurations sharing the same s_y/H value, as their central elements are aligned at $y/D = 0$. This indicates that a parameter other than s_y/H is responsible for the different entrainment pathways observed
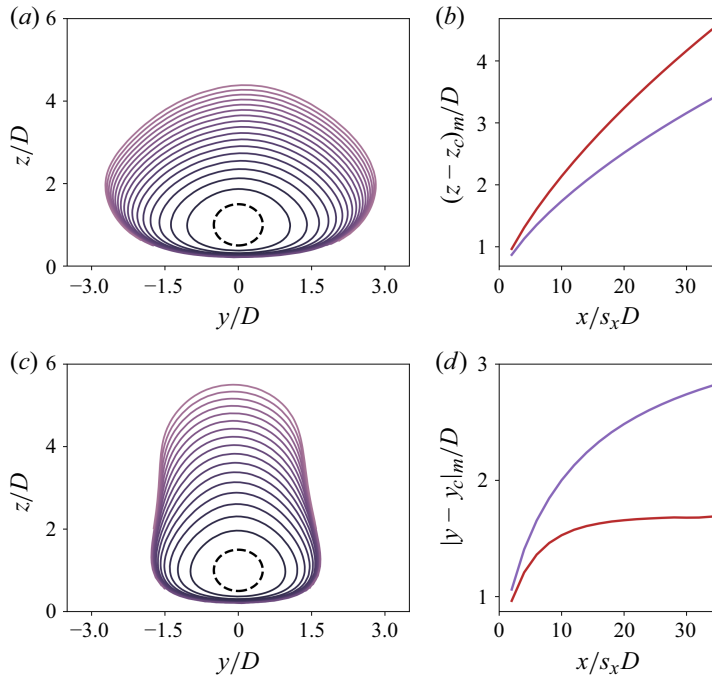
1025 A30-14

Figure 7. Mean energy transport tubes for (*a*) A0-3-3 and (*c*) A0-2-2. Element location is shown by the black dashed line. Tube outlines are plotted at different upstream locations $x = -n s_x D$, with $n = 2, 4, \ldots, 34$. The outline colour gradient indicates the upstream distance from the element, with lighter colours representing locations farther upstream. (*b*) Maximum height and (*d*) maximum spanwise distance at which the MKE is entrained by the element relative to the element centre. Here purple, A0-3-3; red, A0-2-2.

for these cases. As discussed in the previous paragraph, a change in s_a/H – which differs from s_y/H in these configurations – may also influence the MKE entrainment pattern. Specifically, we noted that the cases may fall into different s_a/H regimes, wherein the elements tend to favour either vertical or lateral entrainment. Table 1 highlights this distinction, showing that s_a/H equals 1.25 for S2-5-2 and 1.00 for S4-5-2, which may place them in separate s_a/H regimes. This shift in s_a/H appears to be the driving factor behind the distinct entrainment patterns observed in S2-5-2 and S4-5-2, which ultimately result in the reversal of mean secondary flow polarity seen in figure 4. Thus, we hypothesize that s_a/H is the critical parameter in a multicolumn roughness configuration that governs the polarity of secondary flows. In subsequent subsections, we will disprove s_l/D, staggered configuration and s_w/D as being crucial to the polarity reversal observed in figure 4, thereby reinforcing our hypothesis.

3.2. *Disproving the local spanwise gap (s_l/D) as the critical parameter*

In this subsection, we provide further evidence supporting our conclusion that s_a/H is the critical parameter by showing that s_l/D does not play a decisive role. At a first glance, based on the plots shown in figure 4(*a*,*d*), one might speculate that increasing s_l/D, which results in a significantly larger local spanwise gap between the elements in case S4-5-2 compared with S2-5-2, could influence the preferential fluid pathways locally. A narrower spanwise gap (S2-5-2) may require vertical entrainment of the flow, resulting in a global downdraught over the elements, which may not be necessary when a wider spanwise gap

Case	s_l/D	s_w/D	s_a/H	s_y/H	s_x/h
S2-3-2	2	2	1.417	1.5	4.5
S3.5-3-2	3.5	3.5	1.354	1.5	4.5
S2-5-2	2	4	1.25	1.5	4.5
S3.5-5-2	3.5	7	1.063	1.5	4.5
S2-7-2	2	6	1.083	1.5	4.5
S3.5-7-2	3.5	10.5	0.771	1.5	4.5

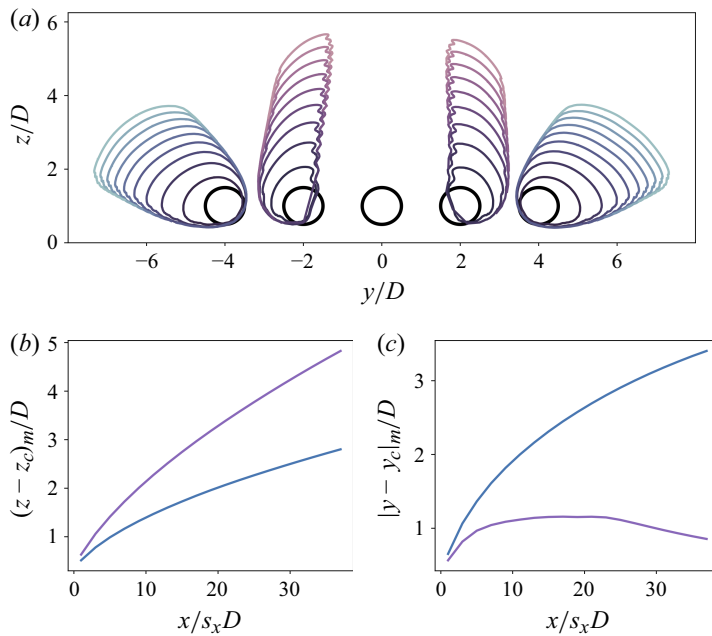Table 3. Suite of simulations for § 3.2. The naming scheme for cases is defined in (2.3). The length scales are the same as in table 1.

Figure 8. (*a*) Mean energy transport tubes for S2-5-2 (purple) and S4-5-2(blue). Elements are shown by the black lines with locations for S2-5-2 and S4-5-2 being $y/D = \{-2, 0, 2\}$ and $y/D = \{-4, 0, 4\}$, respectively. Tube outlines are plotted at different upstream locations $x = -ns_x D$, with $n = 3, 5, \ldots, 37$. The outline colour gradient indicates the upstream distance from the element, with lighter colours representing locations farther upstream. (*b*) Maximum height and (*d*) maximum spanwise distance at which the MKE is entrained by the element relative to the element centre. Here purple, S2-5-2; blue, S4-5-2.

is available for the flow (S4-5-2). To disprove this intuition, we present four new cases along with cases S2-5-2 and S3.5-5-2 considered previously, as outlined in table 3.

Figure 9 presents the pseudocolour plot of vertical velocity for the cases listed in table 3. We first focus on the cases where $s_l/D = 2$. Although these cases share the same s_l/D, they have different s_a/H values due to the increasing number of local columns. For cases S2-3-2 and S2-5-2, distinct downdraughts are observed above the elements. Additionally, the modulation of mean streamwise velocity shows formation of HMPs over the elements and LMPs in the valley. This behaviour contrasts with case S2-7-2, where intermediate secondary flows occur, where the symmetry of the secondary flows breaks down. The modulation of mean streamwise velocity is also markedly different for S2-7-2, as no distinct HMPs or LMPs coincide symmetrically with the elements. Thus, a clear
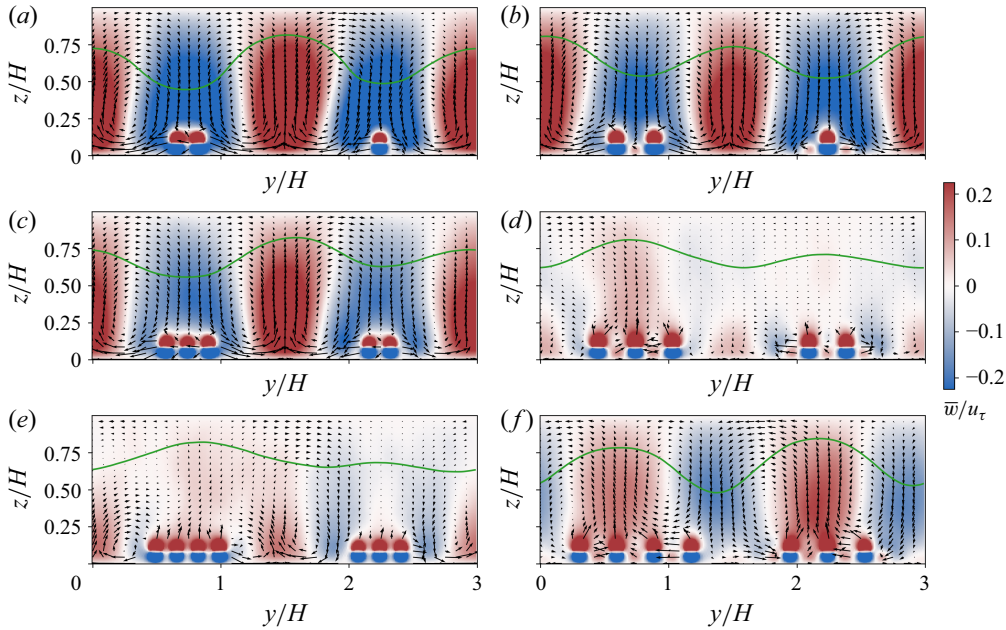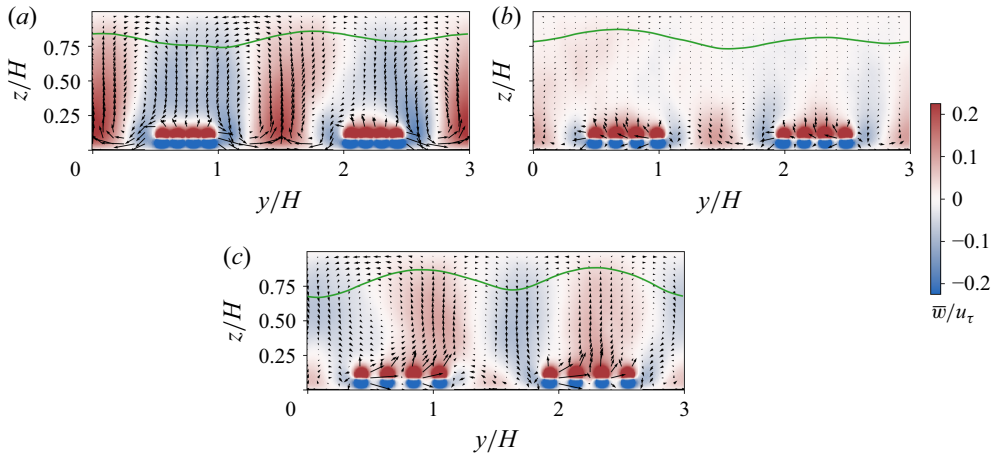
1025 A30-16

Figure 9. Pseudocolour plot of vertical velocity for different cases mentioned in table 3, taken at a streamwise location coinciding with the elements. Here (*a*) S2-3-2, (*b*) S3.5-3-2, (*c*) S2-5-2, (*d*) S3.5-5-2, (*e*) S2-7-2, (*f*) S3.5-7-2. The black arrows indicate the vectors of spanwise and vertical velocity. The green line indicates contour of 95 % of maximum mean streamwise velocity.

transition is observed: from HMPs over the elements in S2-3-2 and S2-5-2 to intermediate secondary flows in S2-7-2, as the value of s_a/H decreases, while keeping s_l/D constant. Similarly, for cases with $s_l/D = 3.5$, we observe a reversal in flow polarity. The flow transitions from HMPs over the elements in S3.5–3-2, to intermediate secondary flows in S3.5-5-2, and to LMPs over the elements in S3.5-7-2, as s_a/H decreases. These six cases can together be ranked in decreasing order of s_a/H as S2-3-2 > S3.5-3-2 > S2-5-2 > S3.5-5-2 $\approx$ S2-7-2 > S3.5-7-2. In this sequence, we observe a progressive transition from HMPs over the elements, to intermediate secondary flows, to LMPs over the elements, independent of changes in the local spanwise gap. Thus, from the observations of different flow response for the same s_l/D (cases S3.5-3-2, S3.5-5-2 and S3.5-7-2) and similar flow response for different s_l/D (cases S2-3-2 and S3.5-3-2), we conclude that s_l/D is not the critical parameter driving the reversal in secondary flow polarity observed in § 3.1. The variations in flow response observed with decreasing s_a/H provide further reinforcement for our conclusion that s_a/H is the key parameter governing this behaviour.

3.3. *Disproving the local element alignment as the critical parameter*

In this subsection, we showcase that the secondary flow polarity reversal observed in § 3.1 is not limited to the staggered configuration within a wider column. To prove this, three new cases are simulated with aligned configuration as outlined in table 4. In these cases, the variation in the parameter s_l/D is kept modest compared with the cases considered in § 3.1 to prevent the formations of local valleys within a wider column. However, by including four elements per wider column, different regimes of s_a/H are obtained despite the limited variation in s_l/D. If the polarity reversal observed in § 3.1 depends solely on

Case	s_l/D	s_w/D	s_a/H	s_y/H	s_x/h
A1.5-8-2	1.5	4.5	1.125	1.5	4.5
A2-8-2	2	6	1	1.5	4.5
A2.5-8-2	2.5	7.5	0.875	1.5	4.5

Table 4. Suite of simulations for § 3.3. The naming scheme for cases is defined in (2.3). The length scales are the same as in table 1.

Figure 10. Pseudocolour plot of vertical velocity for different cases mentioned in table 4, taken at a streamwise location coinciding with the elements. Here (*a*) A1.5-8-2, (*b*) A2-8-2, (*c*) A2.5-8-2. The black arrows indicate the vectors of spanwise and vertical velocity. The green line indicates contour of 95 % of maximum mean streamwise velocity.

s_a/H and is independent of the staggered configuration used, a corresponding shift in the secondary flow response is anticipated for these aligned cases as well.

Figure 10 shows the flow response for these three cases. For the case A1.5-8-2, clear downdraughts are observed over the elements and updraughts are observed within the valley. However, these circulations have only a modest impact on the modulation of mean streamwise velocity, with the formation of weak HMPs over the elements and weak LMPs in the valley. As the ratio s_a/H decreases, intermediate secondary flows are observed for case A2-8-2, where no significant updraughts or downdraughts coincide with the element locations. With a further reduction in s_a/H, pronounced updraughts are observed over the elements, accompanied by the formation of LMPs over the elements and HMPs within the valley. Although fully symmetric secondary flows are not observed in this case, the flow response between cases A1.5-8-2 and A2.5-8-2 is markedly different. These findings indicate that as s_a/H decreases, there is a transition from downdraughts to updraughts over the elements for the aligned configuration, consistent with the observations reported in §§ 3.1 and 3.2 for the staggered configuration. This demonstrates that the observed flow response in § 3.1 is not limited to the local alignment of the elements within a wider column. However, it is important to ensure that the alignment does not create significant local valleys within the wider column. If such valleys form, the very concept of a 'wider column' may break down, which may lead to a disruption in the expected flow behaviour.

1025 A30-18

3.4. *Disproving the width of the wider column (s_w/D) as the critical parameter*

In this subsection, we discuss why the secondary flow polarity reversal observed in § 3.1 is not due to the width of wider columns. For this, we first refer the reader to the cases considered in table 2 and the corresponding energy tube visualization in figure 7. For these cases, there is no change in the width of the columns, as each column contains only a single element. Nevertheless, distinct patterns of MKE entrainment emerge when the parameter s_a/H is varied. This demonstrates that even in the absence of changes in s_w/D, different flow responses can be observed by varying s_a/H.

Next, we discuss the nature of coupling between parameters s_l/D and s_w/D. For cases with an equal number of elements per row, as outlined in table 1, there exists a direct coupling between s_l/D and s_w/D. Specifically, any modification in s_l/D necessitates a corresponding adjustment in s_w/D, precluding independent variation of these parameters. Therefore, s_w/D can be regarded as a local parameter, concerned only with a given wider column. In § 3.2, it is demonstrated that s_l/D does not play a crucial role in determining secondary flow polarity. Given that s_l/D influences only the local interactions within a wider column, this implies that, within the studied spanwise sparsity range (i.e. $s_y/H = 1.5$), the elements' local spanwise columnar interactions are not crucial to the global secondary flow response. This suggests that the different MKE entrainment patterns observed in figure 8 are not critically affected by these local interactions. Since s_w/D also governs local interactions, it can be inferred that the distinct MKE entrainment pathways observed in this figure are not attributable to changes in s_w/D. Therefore, s_w/D is not a critical parameter governing the secondary flow polarity reversal observed in § 3.1. We further add that the coupling between s_l/D and s_a/H is of different nature and is dependent through the parameter s_y/H. Due to this dependence on s_y/H, s_a/H governs interactions between neighbouring wider columns, rather than local interactions within a single wider column. Independent variations in s_l/D and s_a/H can be achieved by changing s_y/H while maintaining the same number of elements per row. Consequently, while it is reasonable to conclude that s_w/D is not a critical parameter – given that s_l/D is non-critical – the same reasoning cannot be applied to s_a/H.

Overall, the analysis presented in this section clearly demonstrates that variations in the parameter s_a/H are the primary driver behind the reversal in secondary flow polarity observed in figure 4. This finding highlights that, in multicolumn configurations, roughness elements located at the edges of the columns can play a decisive role in setting the polarity of secondary flows. While the polarity reversal is evident in the long-time-averaged flow field, the extent to which these structures persist in time remains an open question. In particular, it is unclear whether the presence (figure 4*a*,*d*) or absence (figure 4*b*,*c*) of counter-rotating delta-scale secondary flows in the mean reflects fundamentally different instantaneous dynamics. We address this aspect in the following section.

4. Instantaneous secondary flows and their characteristics

In the previous section, we examined the long-time-averaged secondary flows and the reversal of their polarity. However, certain configurations, such as those shown in figure 4(*b*,*c*), exhibited irregular or seemingly disrupted secondary flows despite prolonged averaging. Since domain-scale secondary flows are artefacts of time-averaging that obscure the underlying transient dynamics (Kevin *et al.* 2017), a closer examination of the unsteady behaviour is needed to better understand these observations. Anderson (2019) demonstrated that secondary flows can undergo instantaneous reversals driven by chaotic and non-periodic dynamics. Similarly, Vanderwel *et al.* (2019) found that
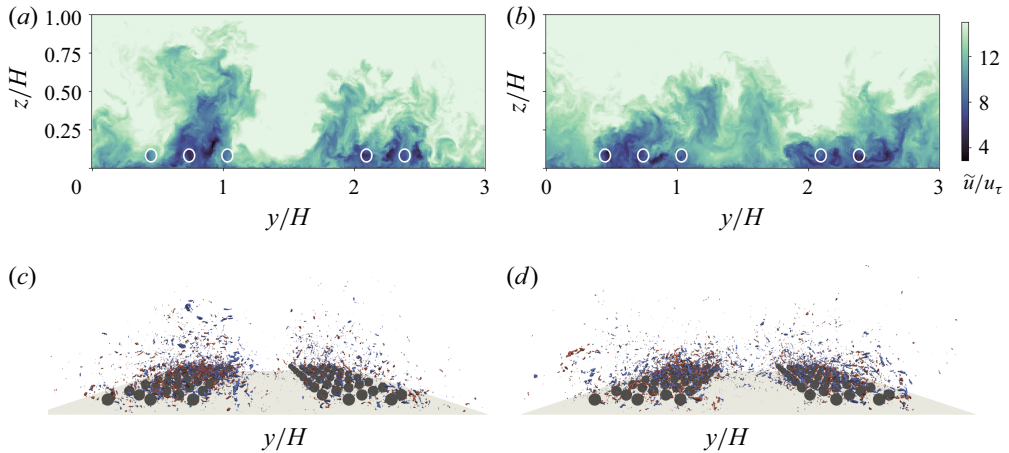
Figure 11. (*a,b*) Pseudocolour plots of normalized streamwise velocity ($\tilde{u}/u_\tau$) at different time steps, taken at a streamwise plane intersecting the element locations for the case S3.5-5-2. White circles indicate element positions. (*c,d*) Visualization of streamwise vortical structures using isosurfaces of signed swirling strength (4 % of maximum λ_{ci}^2). Panels (*c*) and (*d*) correspond to the same time steps as panels (*a*) and (*b*), respectively.

secondary flows emerge from the non-homogeneous distribution of smaller vortices, which meander in location but collectively form large-scale secondary motions in long-time-averaged visualizations. These findings raise the question of whether different roughness arrangements in our study influence the organization of smaller vortices, their meandering behaviour and the propensity for non-periodic reversals in secondary flows. Understanding these tendencies could provide insight into why large-scale, time-averaged secondary flows are observed in some cases but not in others. Therefore, in this section, we analyse the instantaneous structure of secondary flows using flow field visualization, conditional averaging and probability density functions (PDFs) to better understand their transient behaviour. Here, we refer to the instantaneous counterparts of LMPs and HMPs as low-momentum regions (LMRs) and high-momentum regions (HMRs), respectively.

In the analysis that follows, $\widehat{(\cdot)}$ denotes low-pass filtered quantities, and all time scales are normalized by h/u_τ, represented using the superscript $(\cdot)^*$. The conditionally averaged fields are denoted by $\overline{(\cdot)}_c$.

4.1. *Visualization of instantaneous flow field*

In this subsection, we examine the instantaneous flow field behaviour of case S3.5-5-2. Figure 4(*c*) presents the long-time-averaged flow field for this case, and the prominent observations are described briefly here. Unlike the cases in figure 4(*a,d*), which exhibit symmetrical secondary flows, this case displays a pronounced asymmetry, characterized by a strong updraught in the left-hand column and a significantly weaker updraught in the right-hand column. Consequently, symmetrical delta-scale counter-rotating vortices are absent. The time-averaged field also reveals that an updraught remains confined near the wall at the domain centre, with a weak downdraught positioned above it. Additionally, the mean streamwise velocity contour indicates that an HMP aligns with the domain centre, while an LMP is positioned over the roughness elements.

Figure 11(*a,b*) presents two realizations of the instantaneous streamwise velocity for this case, taken approximately 12 large eddy turnovers (H/u_τ) apart. The colour bar is capped so that the velocity values exceeding 80 % of the maximum appear in a uniform light shade, enhancing the visibility of HMRs. In figure 11(*a*), a dominant HMR is

clearly visible at the centre of the domain, while low-momentum fluid remains near the roughness elements and extends upward into the outer layer. However, in figure 11(*b*), an LMR occupies the centre of the domain, penetrating deep into the outer layer. While the low-momentum fluid is always present near the roughness elements due to the drag they impose, these two realizations illustrate that instantaneous secondary circulations can organize themselves to either advect this low-momentum fluid upward or, at a different time step, switch circulation direction and transport it laterally at the centre – despite the roughness arrangement remaining unchanged. Thus, while an HMP appears at the domain centre in the long-time-averaged visualization, this does not imply a continuous presence of HMR at the centre throughout the simulation. Instead, the regions of low- and high-momentum alternate, and what we observe in the long-time-averaged field is the superposition of these alternating structures. Depending on their relative strength and persistence over time, one pathway may appear dominant in the long-time-averaged visualization.

Figure 11(*c,d*) shows the isosurfaces of two-dimensional signed swirl strength, which indicates the strength of local swirling in the streamwise direction. The swirl strength (λ_{ci}) is computed as the imaginary component of the complex eigenvalue of the two-dimensional velocity gradient tensor, computed in the spanwise-wall-normal plane, and is signed based on the direction of vorticity (Zhou *et al.* 1999; Wu & Christensen 2006; Anderson *et al.* 2015*a*). The figure displays isosurfaces corresponding to 4 % of the maximum λ_{ci}^2, a threshold selected to enhance the visualization of stronger circulations while minimizing background noise. In figure 11(*c*), most of the vorticity is concentrated near the elements, while the valley between the arrays exhibits a prominent region of low circulation. In contrast, figure 11(*d*) shows a noticeable increase in vorticity within the valley. Taken together with the streamwise velocity visualizations, these observations indicate that LMRs are associated with strong streamwise circulations, whereas HMRs tend to suppress them. This observation aligns with the findings in the literature, where it is reported that LMPs exhibit stronger random fluctuations, while HMPs remain comparatively calmer (Barros & Christensen 2014; Anderson *et al.* 2015*a*; Kevin *et al.* 2017; Vanderwel *et al.* 2019). Additional analysis of instantaneous vortices (not shown) reveals that, across all cases listed in table 1, the largest instantaneous vortex is approximately an order of magnitude smaller than the delta-scale vortex. This analysis also indicates that larger instantaneous circulations generally tend to be weaker, while stronger circulations are typically confined to smaller spatial regions. These findings confirm that delta-scale vortices do not exist instantaneously but instead arise as a consequence of time-averaging.

The observations presented in this subsection give rise to three key questions.

(i) For how long does a given region of low- or high-momentum persist at the centre?
(ii) How frequently do the regions switch between one another?
(iii) Is this behaviour universal, or does it depend on the roughness arrangement?

Exploring these questions is essential to understanding why some cases exhibit symmetrical secondary flows, while others appear disrupted. The next subsection investigates these aspects in greater detail, shedding light on the underlying flow dynamics.

4.2. *Conditional averaging of instantaneous flow field*

In this subsection, we investigate the conditionally averaged flow fields for the cases listed in tables 1 and 3. As discussed in the previous subsection, the HMR and the LMR can both occur at the domain centre at different instances, indicating reversals in

the swirling direction of the secondary flows. Since downdraughts and updraughts serve as key indicators for the presence of HMRs and LMRs, respectively, we categorize the instantaneous flow into two distinct events, based on the relative occurrence of updraughts and downdraughts at the domain centre. For this conditional averaging, velocity data from eight spanwise locations are considered: four located closest to the centre of the domain, and two each near the edges in the spanwise direction. These edge locations also represent valleys between elements due to the periodic boundary condition. At each of these locations, vertical velocity values from the entire streamwise and vertical extent are included, resulting in approximately 885 000 grid points at which updraught and downdraught occurrences are evaluated for each time step. Consequently, two distinct averaged velocity fields are generated: one representing the event when updraughts outnumber downdraughts, and the other corresponding to the event when downdraughts predominate.

To formalize this classification, let $w(\boldsymbol{x}_i, t)$ be the instantaneous vertical velocity at grid point $\boldsymbol{x}_i$ and time t, with $\mathcal{D}$ denoting the set of diagnostic grid points. At each time instant t, the number of updraught and downdraught points is computed as

$$N_{up}(t) = \#\{\boldsymbol{x}_i \in \mathcal{D} \mid w(\boldsymbol{x}_i, t) > 0\},$$
$$N_{down}(t) = \#\{\boldsymbol{x}_i \in \mathcal{D} \mid w(\boldsymbol{x}_i, t) \leqslant 0\}. \tag{4.1}$$

The flow field at time t is classified as updraught-dominated if $N_{up}(t) > N_{down}(t)$ and as downdraught-dominated otherwise. The corresponding conditional averages are then defined as

$$\overline{u}_{i_{c+}}(\boldsymbol{x}) = \frac{1}{T_{up}} \sum_{t\,:\,N_{up}(t)>N_{down}(t)} \tilde{u}_i(\boldsymbol{x}, t)\,,$$
$$\overline{u}_{i_{c-}}(\boldsymbol{x}) = \frac{1}{T_{down}} \sum_{t\,:\,N_{down}(t)\geq N_{up}(t)} \tilde{u}_i(\boldsymbol{x}, t)\,, \tag{4.2}$$

where T_{up} and T_{down} are the number of time instants satisfying each condition.

Figure 12 presents the conditionally averaged vertical velocity fields for the cases listed in table 1. Figure 12(*a,c,e,g*), corresponds to events where updraughts outnumber downdraughts at the domain centre, while figure 12(*b,d,f,h*), depicts events dominated by downdraughts. The vertical bar on the left-hand side of each row indicates the percentage of simulation time for which each specific event occurs, with the extent of red colour denoting dominant updraughts and blue representing dominant downdraughts. It is evident that in all cases – including those where symmetrical secondary flows with a dominant polarity were observed – the updraughts and downdraughts do not persist for the entire duration of the simulation. For instance, in case S2-5-2, an updraught exists at the domain centre for 93 % of the simulation time, while downdraughts dominate 7 % of the time. As a result, the conditionally averaged field shown in figure 12(*a*) closely resembles the long-time averaged field in figure 4(*a*), as the events with opposite polarity lack sufficient temporal persistence to leave a significant imprint on the long-time averaged flow field. As the parameter s_a/H is decreased, moving to the case S2.75-5-2, events with dominant downdraughts become substantially more frequent, constituting 46.6 % of the simulation time steps, while updraughts persist for the remaining 53.4 % of the time. In periods where downdraughts dominate, the streamwise velocity clearly exhibits strong spanwise modulation, with HMPs appearing at the domain centre and LMPs aligned over the roughness elements. In contrast, when updraughts dominate, the modulation is notably weaker, with weak LMPs near the domain centre and weak HMPs
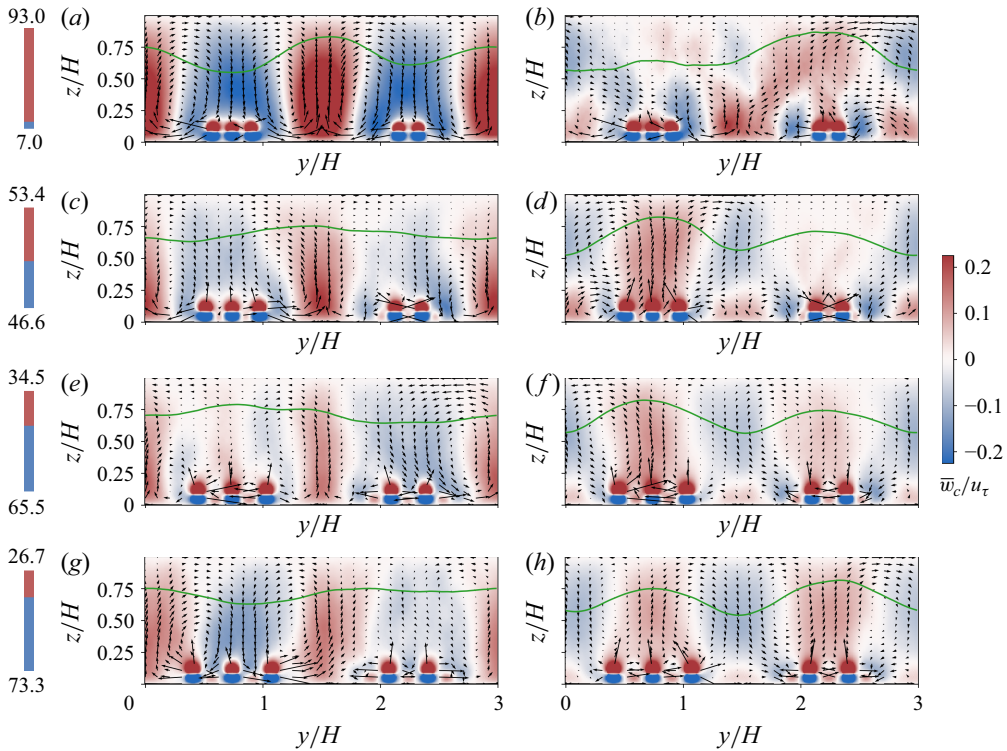
Figure 12. Conditionally averaged pseudocolour plots of vertical velocity at a streamwise location aligned with the elements for the cases listed in table 1: (*a,b*) S2-5-2, (*c,d*) S2.75-5-2, (*e,f*) S3.5-5-2, (*g,h*) S4-5-2. Panels (*a*), (*c*), (*e*) and (*g*) correspond to events where updraughts outnumber downdraughts, while panels (*b*), (*d*), (*f*) and (*h*) represent events dominated by downdraughts. The vertical bar on the left-hand side of each row indicates the percentage of time updraughts were dominant (red, with numerical value at the top) and the percentage of time downdraughts were dominant (blue, with numerical value at the bottom). Black arrows indicate the vectors of spanwise and vertical velocity. The green line indicates contour of 95 % of maximum mean streamwise velocity.

near the elements. This observation is significant because, in the long-time averaged field shown in figure 4(*b*), an HMP appears at the domain centre, despite the updraught (and its associated LMP) persisting longer. This highlights that the long-time average may not always reflect the flow structures that are most frequently present throughout the simulation. Another interesting observation for this case is the reversal of flow pathways at the roughness elements. Specifically, figure 12(*c*) shows downdraughts clearly aligned with the elements, while figure 12(*d*) shows updraughts aligned over these arrays. This behaviour differs from the findings of Vanderwel *et al.* (2019), who reported that for flow over streamwise-aligned ridges, LMRs remained anchored to elevated surface regions, extending deep into the boundary layer as narrow and meandering streaks. We attribute this discrepancy to differences in the physical nature of roughness elements and the presence of significant streamwise gap in our roughness configuration. Overall, despite both the conditionally averaged flow fields showcasing the presence of delta scale vortices, as no event has dominant presence throughout the simulation, the long-time averaged visualization shows seemingly disrupted secondary flows. Further decreasing s_a/H results in case S3.5-5-2, where downdraughts become even more frequent, dominating approximately 65.5 % of the simulation duration compared with 34.5 % for updraughts. Similar to the previous case, downdraught-dominated events strongly modulate streamwise

velocity, while updraught-dominated events exhibit only weak modulation. Interestingly, all delta-scale vortices observed in the conditional averages for this case rotate in a anticlockwise direction. This explains why a prominent anticlockwise delta-scale vortex appears clearly in the long-time averaged visualization (figure 4*c*), even though the rest of the flow appears somewhat disrupted due to the lack of persistent dominance of one particular pathway. This is likely due to the dominance of one-sided large-scale rotational motions in this configuration, a feature previously identified by Kevin *et al.* (2017). Finally, in case S4-5-2, where clear delta-scale secondary flows and dominant pathways appear in the long-time averaged visualization, downdraughts dominate at the domain centre for approximately 73 % of the simulation. However, the reversed secondary flow pattern remains less symmetric than in case S3.5-7-2 (figure 9*f*), where downdraughts dominate approximately 95 % of the simulation time, resulting in a symmetrical long-time averaged flow pattern. Overall, as s_a/H is progressively decreased, we observe a consistent shift towards downdraught dominance at the domain centre. The configurations transition from exhibiting a strong central updraught to a pronounced central downdraught, eventually reaching a level where this reversal is clearly evident in the long-time-averaged flow field.

From the analysis so far, it is abundantly clear that for most of the secondary flow simulations, the updraughts and downdraughts, and the associated LMRs and HMRs, do not remain stable and may interchange with one another. However, it remains unclear whether these reversals occur in a periodic manner or follow a more chaotic, non-periodic pattern. To investigate this, figure 13 marks the starting time step where a particular updraught or downdraught event occurs and the marker's extent on *y* axis indicates the duration for which that event persists. The analysis is conducted for the cases mentioned in table 1 along with the case S3.5-7-2 in table 3 to emphasize dynamics of a case where downdraughts dominate at the centre of the domain for the majority of the simulation.

For case S2-5-2, we observe that the updraughts at the domain centre are relatively stable and can persist continuously for extended durations. In contrast, downdraughts occur infrequently and in a non-periodic manner, and they are typically short-lived. For the intermediate cases shown in figure 13(*b,c*), the average temporal extent of both updraughts and downdraughts is significantly reduced. The vertical axis scale is adjusted individually for each subplot in the figure to enhance visual clarity. In these cases, the relative occurrence of updraughts and downdraughts at the domain centre appears roughly balanced, with the exception of two long-duration updraughts events in case S2.75-5-2. Due to the reduced persistence of individual events, these intermediate configurations undergo frequent, non-periodic reversals. As a result, the secondary flow patterns appear disrupted in the long-time-averaged visualizations. As s_a/H decreases further, in cases such as S4-5-2 and S3.5-7-2, we find that downdraughts at the domain centre begin to stabilize and persist for longer durations compared with updraughts. With downdraughts sustaining for extended periods, reversals occur less frequently, and the long-time-averaged flow fields exhibit greater symmetry, with clearly organized LMPs and HMPs.

Figure 14 provides a quantitative assessment of the visual observations discussed above. This figure includes all cases listed in tables 1 and 3, arranged in decreasing order of s_a/H. The percentage existence of updraught and downdraught events refers to the fraction of the simulation during which a particular event is dominant. The average time of existence denotes the mean duration for which a given event persists continuously. To avoid the influence of very short-lived events on the average time of existence, only the events persisting for $t^* > 1$ are considered. As shown in figure 14(*a*), cases in which one event exists for more than 2.5 times the duration of the other tend to exhibit a dominant
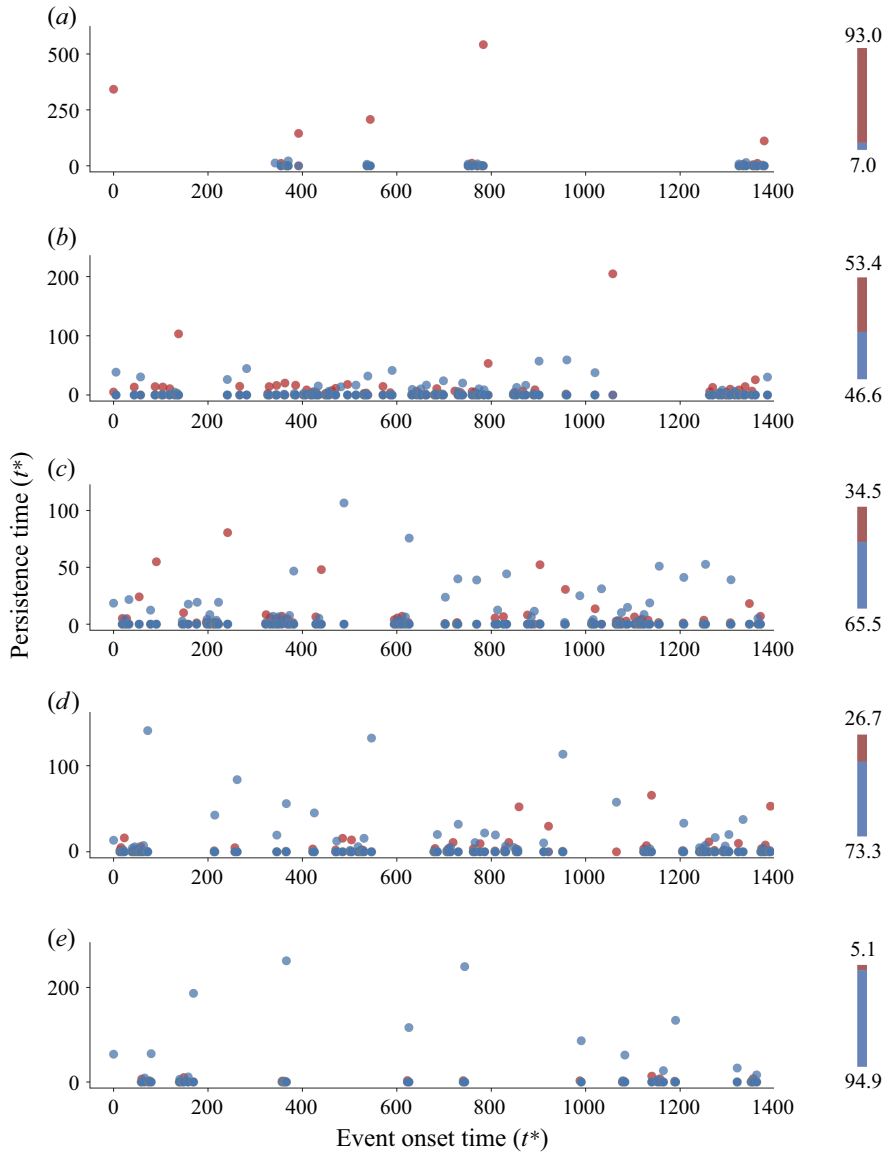
Figure 13. Temporal persistence of updraught and downdraught events for cases: (*a*) S2-5-2, (*b*) S2.75-5-2, (*c*) S3.5-5-2, (*d*) S4-5-2, (*e*) S3.5-7-2. The red colour denotes a net updraught at the domain centre, while the blue colour denotes a net downdraught. The vertical bar on the right-hand side of each row indicates the percentage of time updraughts were dominant (red, with numerical value at the top) and the percentage of time downdraughts were dominant (blue, with numerical value at the bottom).

polarity in the long-time averaged flow field, accompanied by clear delta-scale vortices. In contrast, intermediate cases show roughly equal presence of both polarities, with no single event significantly dominating the other. A similar trend is observed in the average time of existence. For the intermediate cases, both events persist for nearly equal durations, whereas in cases with a dominant polarity, the dominant event lasts at least twice as long as the non-dominant one.
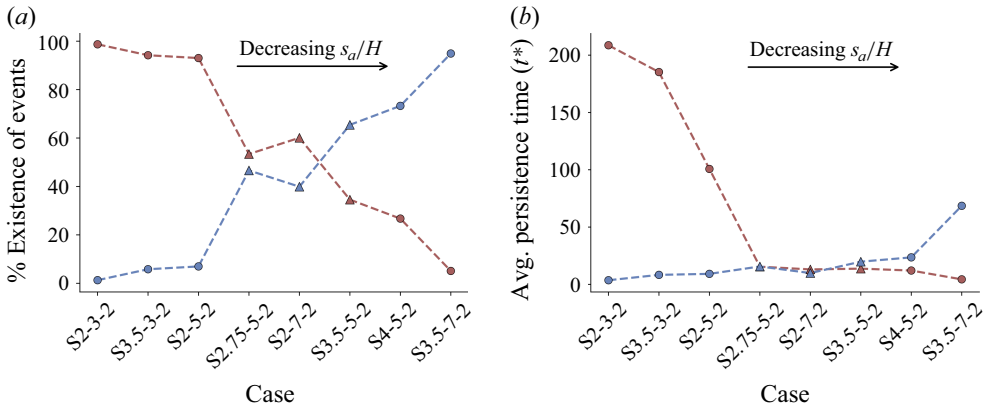
Figure 14. (*a*) Percentage occurrence of updraught and downdraught events and (*b*) average persistence time for the cases outlined in tables 1 and 3. The red colour denotes a net updraught at the domain centre, while the blue colour denotes a net downdraught. Circles indicate cases exhibiting a dominant polarity in long-time-average visualization, whereas triangles indicate cases with disrupted secondary flows in long-time-average visualization. The cases are arranged in decreasing order of s_a/H.

In conclusion, the analysis presented in this subsection reveals a clear transitional behaviour as the parameter s_a/H decreases from case S2-5-2 to case S3.5-7-2. For the cases outlined in tables 1 and 3, it is observed that when $s_a/H \gtrsim 1.2$, delta-scale secondary flows emerge with LMPs and associated updraughts aligned at the domain centre. These updraughts persist for the majority of the simulation time, and although reversals can occur, they are brief and contribute negligibly to the long-time averaged flow field. When the cases lie in the regime $1.2 \gtrsim s_a/H \gtrsim 1$, the updraughts at the domain centre become increasingly unstable and do not sustain for longer periods during the simulations. As a result, the reversal occurs much more frequently, and both events appear to be short-lived. As no particular event significantly dominates the other in this regime, the secondary flows appear to be disrupted in the long-time average visualization. However, for these cases, delta-scale vortices can still be observed in the conditionally averaged flow field, as shown in figure 12(*c,d*). When s_a/H is reduced further such that the cases lie in the regime $s_a/H \lesssim 1$, the HMPs and associated downdraughts at the domain centre begin to dominate and sustain for longer durations. As a result, the propensity of the system for reversals decreases, and we again observe delta scale secondary flows with a prominent alignment of pathways in the long-time average visualization.

4.3. *Characterization of instantaneous vertical velocity distribution*

In the previous subsection, we classified events based on the sign of the vertical velocity at grid points located at the domain centre, thereby distinguishing between updraughts and downdraughts. While this approach provided valuable insight into the switching behaviour between these events at the domain centre, it did not capture variations in the magnitude of vertical velocity within individual events. As observed in figure 13, different roughness configurations influence the stability of the events sustained at the domain centre. This raises the question of whether the time series of vertical velocity exhibits distinct signatures depending on whether a dominant event – either updraught or downdraught – is sustained at the domain centre, or whether the flow frequently switches between the two. Therefore, in this subsection, we analyse the temporal evolution of vertical velocity to gain a deeper understanding of its dynamics during updraught and downdraught events.
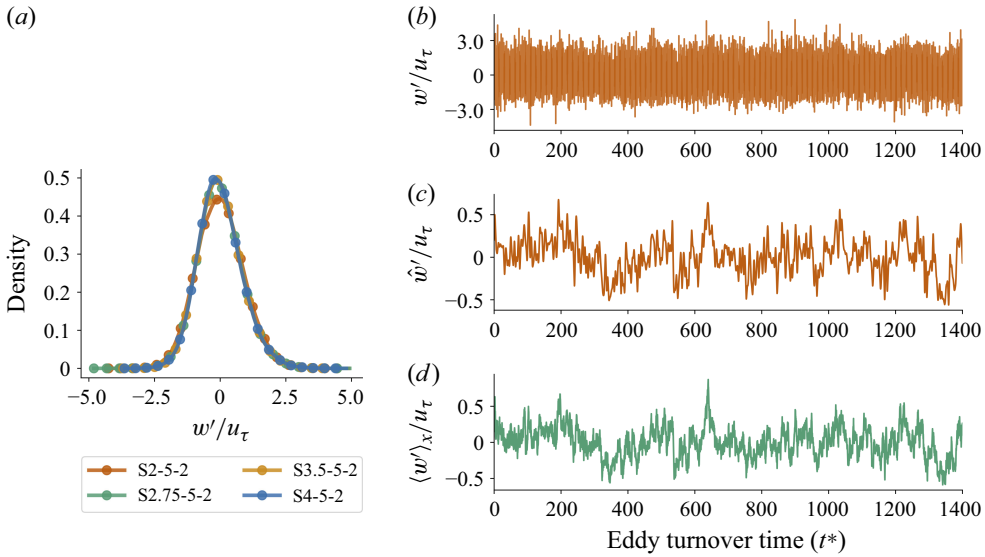
Figure 15. (*a*) Probability density functions of the time series of vertical velocity fluctuations for the cases listed in table 1. Data are sampled at two streamwise positions: the location of the first row of elements (solid lines), and the midpoint between the first and second element rows (circles). In both cases, the spanwise and vertical location of the sampling point corresponds to the centre of the Y–Z plane, i.e. $y = L_y/2$ and $z = H/2$. (*b*) Time series of vertical velocity fluctuations for case S2-5-2, sampled at a grid point aligned with the first element row. (*c*) Low-pass filtered version of the signal shown in (*b*). (*d*) Signal sampled and averaged over every x location at $y = L_y/2$ and $z = H/2$.

Figure 15(*a*) presents the PDFs of the time series of vertical velocity fluctuations for the cases listed in table 1. To assess the influence of streamwise heterogeneity introduced by the roughness arrangement, vertical velocity time signals are sampled at two streamwise locations: one coinciding with the first row of elements, and the other situated at the midpoint between the first and second element rows. The spanwise position of the sampling point is fixed at the domain centre (i.e. $y = L_y/2$), and the vertical position is located at half the half-channel height (i.e. $z = H/2$). As seen from the figure, the PDFs at the two streamwise locations exhibit a high degree of similarity, suggesting that the streamwise heterogeneity in the roughness layout does not significantly affect the statistical properties of vertical velocity at this particular spanwise location and height.

In this figure, the case S2-5-2 exhibits a distinctly broader PDF – indicating a higher standard deviation – while the PDFs for the other cases appear remarkably similar. The similarity between the intermediate cases (S2.75-5-2 and S3.5-5-2) and S4-5-2 is intriguing, as it suggests that the frequent pathway reversals characterizing the intermediate cases do not leave a distinct imprint on the temporal statistics of vertical velocity, compared with cases with a persistent central pathway and infrequent reversals. Instead, the broader distribution observed for S2-5-2, along with the monotonic (albeit modest) decrease in standard deviation across the other cases, implies that the intensity of fluctuations is primarily governed by how long the flow locally maintains an updraught—typically associated with stronger turbulent activity – or a downdraught, which tends to exhibit weaker fluctuations.

Figure 15(*b*) shows the time series of vertical velocity fluctuations for case S2-5-2. While the signal exhibits strong turbulent fluctuations, it also reveals an underlying
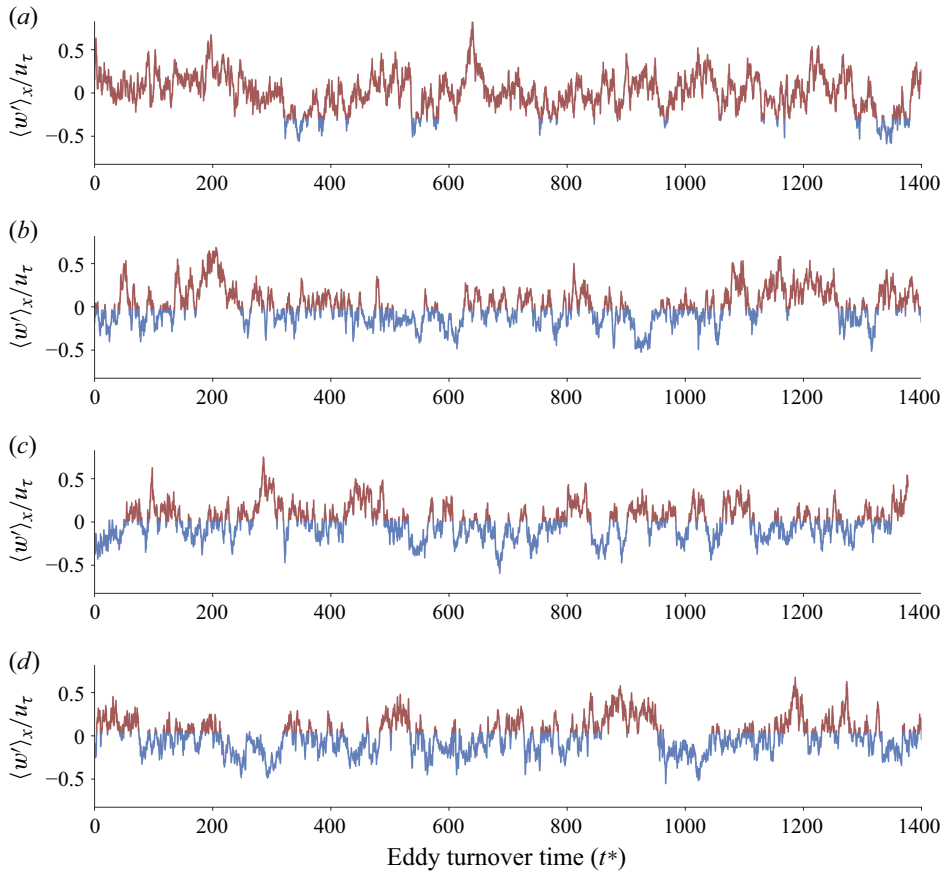
Figure 16. Time series of vertical velocity fluctuations that are sampled and averaged over every x location at $y = L_y/2$ and $z = H/2$, for cases: (*a*) S2-5-2, (*b*) S2.75-5-2, (*c*) S3.5-5-2, (*d*) S4-5-2. The red colour denotes a positive vertical velocity ($\langle \overline{w} \rangle_x + \langle w' \rangle_x > 0$) while the blue colour denotes a negative vertical velocity.

low-frequency modulation. To isolate and examine this low-frequency behaviour, we apply the maximal overlap discrete wavelet transform using a Coiflet2 wavelet. The maximal overlap discrete wavelet transform smooth component acts as a zero-phase, shift-invariant low-pass filter, preserving the temporal alignment of the low-frequency content with the original signal (Percival & Mofjeld 1997). The support of the scaling function used for filtering spans approximately 45 000 time steps ($t^* = t u_\tau / h \approx 9.1$), applied to a signal with a total duration of 7 000 000 time steps ($t^* = 1417.5$). The resulting low-pass filtered signal is shown in figure 15(*c*). Figure 15(*d*) presents the streamwise-averaged vertical velocity fluctuations, obtained by averaging the signal across all the streamwise grid points at $y = L_y/2$ and $z = H/2$ at each time step. The resulting time series closely resembles the low-pass filtered signal derived from a single point, indicating that the streamwise averaging operation at this spanwise and vertical location effectively preserves the long-time variations in the vertical velocity fluctuations observed during the simulation. Therefore, to mitigate sensitivity to sampling location, we hereafter focus on the streamwise-averaged vertical velocity signal.

Figure 16 shows the streamwise-averaged vertical velocity fluctuations at $y = L_y/2$ and $z = H/2$ for the cases listed in table 1. To enable direct comparison with figure 13, which illustrates the time-dependent switching of updraught and downdraught events,
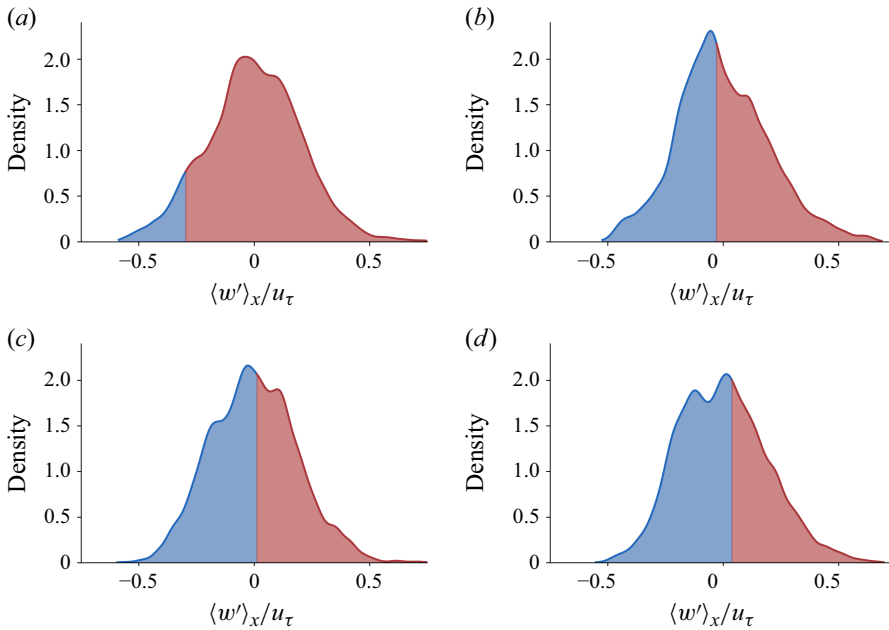
1025 A30-28

Figure 17. Probablity density function of time series of vertical velocity fluctuations that are sampled and averaged over every x location at $y = L_y/2$ and $z = H/2$, for cases: (*a*) S2-5-2, (*b*) S2.75-5-2, (*c*) S3.5-5-2, (*d*) S4-5-2. The red region denotes a positive vertical velocity ($\langle \overline{w} \rangle_x + \langle w' \rangle_x > 0$) while the blue region denotes a negative vertical velocity.

the signal is colour-coded such that red indicates regions where the vertical velocity is positive (i.e. $\langle \overline{w} \rangle_x + \langle w' \rangle_x > 0$), while blue indicates regions where it is negative. From the figure, it is evident that all four cases exhibit similar low-frequency, periodic modulations in the vertical velocity, with the standard deviation remaining within 10 % across all cases. Although conditional averaging previously indicated that the updraught at the domain centre is relatively stable in case S2-5-2, persisting for long durations with infrequent reversals, this stability of the event does not necessarily correspond to a vertical velocity signal with lower temporal variability. As seen in figure 16(*a*), the vertical velocity remains predominantly positive for extended periods, but its magnitude continues to undergo quasiperiodic oscillations, similar to those observed in the other cases (figure 16*b*–*d*). However, because these oscillations mostly occur within the positive regime, they do not manifest as reversals in the conditionally averaged statistics. In contrast, for the intermediate cases (S2.75-5-2 and S3.5-5-2), the vertical velocity oscillations frequently cross zero, leading to repeated sign changes. This is primarily due to the mean vertical velocity at this location being close to zero. Thus, the more frequent switching observed in figure 13(*c*), relative to figure 13(*a*), reflects the near-neutral mean state rather than an inherently more chaotic fluctuation pattern. In fact, as noted earlier in the discussion of figure 15, updraught-dominated regions are associated with stronger turbulent fluctuations. Therefore, case S2-5-2, which sustains more persistent updraughts, exhibits higher overall variance in vertical velocity compared with the intermediate cases, despite appearing less dynamic in terms of switching between updraughts and downdraughts.

Figure 17 shows the PDFs of the streamwise-averaged vertical velocity fluctuations discussed above. The PDFs are colour-coded such that red corresponds to regions where

the vertical velocity is positive (i.e. $\langle \overline{w} \rangle_x + \langle w' \rangle_x > 0$), and blue corresponds to negative vertical velocity. In contrast to the unimodal distributions observed in figure 15, the streamwise-averaged PDFs in this figure reveal a clear multimodal character across all cases. For cases S2-5-2 and S4-5-2, which exhibit a dominant polarity in the long-time-averaged flow field, the prominent modes lie predominantly on one side of the mean: positive for S2-5-2 and negative for S4-5-2. However, for the intermediate cases (S2.75-5-2 and S3.5-5-2), the modes are distributed on both sides of the mean, reflecting frequent transitions between updraught- and downdraught-dominated states. These observations imply that secondary circulations are inherently unsteady, regardless of whether the time-averaged flow exhibits a persistent polarity or not. In all cases, the vertical velocity signal fluctuates between multiple preferred states, as evidenced by the modal structure of the PDFs. This behaviour persists even in flows that do not visibly exhibit frequent switching, indicating that temporal variability in the vertical momentum transport is a fundamental feature of the secondary flow dynamics.

5. Conclusion

In this study, we conducted a series of LES to examine the behaviour of secondary flows induced by multicolumn roughness configurations. Each column consisted of multiple, individually resolved roughness elements arranged in both the streamwise and spanwise directions. Wind turbines were used as the roughness elements to represent flow through porous media. The local spanwise gap between the elements as well as the number of element columns were systematically varied to construct a range of roughness configurations. Subsequently, we analysed how these geometric modifications influenced the polarity and temporal dynamics of the resulting secondary flows.

The study first examined the time-averaged characteristics of secondary flows in § 3. The key findings from this section are summarized below.

(i) The analysis established that the parameter s_a/H – defined as the ratio of the spanwise gap between roughness elements in adjacent columns to the boundary layer height – plays a critical role in determining the polarity of secondary flows in multicolumn roughness configurations.

(ii) Using the energy tube framework introduced by Meyers & Meneveau (2013), we demonstrated how variations in s_a/H influence the entrainment pathways of the MKE. The geometry of these energy tubes was shown to encode clear information about the streamwise circulation patterns associated with secondary flows. This methodology offers a valuable alternative to the traditional TKE budget analysis for secondary flows, particularly in complex roughness arrangements where symmetry-based simplifications in the TKE budget are not applicable.

(iii) Based on the value of s_a/H, the cases in this study can be categorized into three distinct regimes. When $s_a/H \gtrsim 1.2$, the long-time averaged flow field showed delta-scale secondary flows with HMPs and the corresponding downdraughts aligned with the elements, and LMPs and associated updraughts aligned with the valley between the elements. When $1.2 \gtrsim s_a/H \gtrsim 1$, the secondary flow structures in the long-time-averaged field appear disrupted, lacking the presence of symmetrical delta-scale vortices. For $s_a/H \lesssim 1$, the long-time-averaged field once again shows delta-scale secondary flows, but with a polarity reversal: LMPs and associated updraughts are now aligned with the element columns, while HMPs and associated downdraughts appear over the valleys.

To uncover why different s_a/H regimes give rise to either coherent or disrupted secondary flows in the long-time-averaged fields, we examined the instantaneous flow behaviour in §4, focusing on the transient mechanisms that are obscured by time averaging. The key findings from this section are summarized below.

(i) Across all the cases, regardless of the s_a/H regime, the updraughts and downdraughts, along with their associated LMRs and HMRs, respectively, do not remain permanently aligned with the roughness topography. Instead, they alternate between each other in a chaotic, non-periodic manner over time.

(ii) In the regimes $s_a/H \gtrsim 1.2$ and $s_a/H \lesssim 1$, where a dominant polarity of secondary flow is observed in the long-time-averaged visualizations, the dominant vertical motion tends to persist for the majority of the simulation. While reversals may still occur, they are generally infrequent and short-lived. In contrast, in the intermediate regime ($1.2 \gtrsim s_a/H \gtrsim 1$), where the secondary flow structures appear disrupted in the long-time-averaged field, neither vertical event dominates over time. Instead, frequent reversals occur, and both the updraught and downdraught events tend to persist for similar durations, indicating that the disrupted appearance arises due to the comparable strength and temporal prevalence of the competing vertical motions. Nonetheless, delta-scale secondary structures with opposite rotational directions can be observed for these cases in the conditionally averaged flow field.

(iii) Analysis of the vertical velocity time series showed that frequent switching between the vertical events does not translate into a qualitatively different temporal signal. Even in cases with a persistent event, the low-frequency signal of vertical velocity exhibits similar quasiperiodic oscillations to those seen in cases with frequent reversals. This showed that the increased frequency of switching between the events reflects a near-zero mean vertical velocity rather than an inherently more chaotic fluctuation pattern.

(iv) The PDFs of streamwise-averaged vertical velocity exhibited a clear multimodal structure across all cases, indicating that the secondary circulations are inherently unsteady and that the vertical velocity fluctuates between multiple preferred states. In cases with a dominant polarity, these preferred states share the same sign of vertical velocity, while in intermediate cases, they span both positive and negative values, indicating that neither event dominates and both play an important role in shaping the flow dynamics.

(v) Overall, the analysis in this section showed that the temporal variability in the vertical momentum transport is a fundamental feature of the secondary flow dynamics.

Taken together, these findings provide a comprehensive picture of how the geometric arrangement of roughness elements governs not only the mean structure but also the temporal behaviour of secondary flows. The specific s_a/H regimes and the values of the length scales reported in §3 are expected to be sensitive to the specific geometry and physical characteristics of the roughness elements, as these directly influence the MKE entrainment pathways and, in turn, the global polarity of the secondary flows. By contrast, the insights into the instantaneous structure and temporal dynamics appear to reflect more general features of roughness-induced secondary flows. The dynamical behaviours documented in this study are consistent with the trends observed in prior investigations conducted over markedly different surface types (Kevin *et al.* 2017; Anderson 2019; Vanderwel *et al.* 2019; Wangsawijaya *et al.* 2020).

Declaration of interests. The authors report no conflict of interest.

REFERENCES

ACHARYA, M., BORNSTEIN, J. & ESCUDIER, M.P. 1986 Turbulent boundary layers on rough surfaces. *Exp. Fluids* **4**, 33–47.

ALBERTSON, J.D. & PARLANGE, M.B. 1999*a* Natural integration of scalar fluxes from complex terrain. *Adv. Water Resour.* **23**, 239–252.

ALBERTSON, J.D. & PARLANGE, M.B. 1999*b* Surface length scales and shear stress: Implications for land-atmosphere interaction over complex terrain. *Water Resour. Res.* **35**, 2121–2132.

ANDERSON, W. 2019 Non-periodic phase-space trajectories of roughness-driven secondary flows in high-re-boundary layers and channels. *J. Fluid Mech.* **869**, 27–84.

ANDERSON, W., BARROS, J.M., CHRISTENSEN, K.T. & AWASTHI, A. 2015*a* Numerical and experimental study of mechanisms responsible for turbulent secondary flows in boundary layer flows over spanwise heterogeneous roughness. *J. Fluid Mech.* **768**, 316–347.

ANDERSON, W., LI, Q. & BOU-ZEID, E. 2015*b* Numerical simulation of flow over urban-like topographies and evaluation of turbulence temporal attributes. *J. Turbul.* **16**, 809–831.

BARROS, J.M. & CHRISTENSEN, K.T. 2014 Observations of turbulent secondary flows in a rough-wall boundary layer. *J. Fluid Mech.* **748**, R1–R13.

BOU-ZEID, E., MENEVEAU, C. & PARLANGE, M.B. 2005 A scale-dependent Lagrangian dynamic model for large eddy simulation of complex turbulent flows. *Phys. Fluids* **17**, 025105.

BRAGG, M.B., BROEREN, A.P. & BLUMENTHAL, L.A. 2005 Iced-airfoil aerodynamics. *Prog. Aerosp. Sci.* **41**, 323–362.

COLEBROOK, C.F., WHITE, C.M. & TAYLOR, G.I. 1937 Experiments with fluid friction in roughened pipes. *Proc. R. Soc. Lond. A Math. Phys. Sci.* **161** (906), 367–381.

CALAF, M., MENEVEAU, C. & MEYERS, J. 2010 Large eddy simulation study of fully developed wind-turbine array boundary layers. *Phys. Fluids* **22**, 015110.

CANUTO, C., HUSSAINI, M.Y., QUARTERONI, A. & ZANG, T.A. 2007 *Spectral Methods: Evolution to Complex Geometries and Applications to Fluid Dynamics*. Springer Science & Business Media.

CASTRO, I.P., KIM, J.W., STROH, A. & LIM, H.C. 2021 Channel flow with large longitudinal ribs. *J. Fluid Mech.* **915**, A92.

CHAMECKI, M., MENEVEAU, C. & PARLANGE, M.B. 2009 Large eddy simulation of pollen transport in the atmospheric boundary layer. *J. Aerosol. Sci.* **40**, 241–255.

CHUNG, D., MONTY, J.P. & HUTCHINS, N. 2018 Similarity and structure of wall turbulence with lateral wall shear stress variations. *J. Fluid Mech.* **847**, 591–613.

CLAUS, J., COCEAL, O., THOMAS, T.G., BRANFORD, S., BELCHER, S.E. & CASTRO, I.P. 2012 Wind-direction effects on urban-type flows. *Boundary-Layer Meteorol.* **142**, 265–287.

COCEAL, O., THOMAS, T.G., CASTRO, I.P. & BELCHER, S.E. 2006 Mean flow and turbulence statistics over groups of urban-like cubical obstacles. *Boundary-Layer Meteorol.* **121**, 491–519.

CORTINA, G., SHARMA, V., TORRES, R. & CALAF, M. 2020 Mean kinetic energy distribution in finite-size wind farms: a function of turbines' arrangement. *Renew. Energy* **148**, 585–599.

FANG, J. & PORTÉ-AGEL, F. 2015 Large-eddy simulation of very-large-scale motions in the neutrally stratified atmospheric boundary layer. *Boundary-Layer Meteorol.* **155**, 397–416.

GIOMETTO, M.G., CHRISTEN, A., MENEVEAU, C., FANG, J., KRAFCZYK, M. & PARLANGE, M.B. 2016 Spatial characteristics of roughness sublayer mean flow and turbulence over a realistic urban surface. *Boundary-Layer Meteorol.* **160**, 425–452.

GRIGSON, C. 1992 Drag losses of new ships caused by hull finish. *J. Ship Res.* **36**, 182–196.

HINZE, J.O. 1967 Secondary currents in wall turbulence. *Phys. Fluids* **10**, S122–S125.

HORA, G.S. & GIOMETTO, M.G. 2024 Surrogate modeling of urban boundary layer flows. *Phys. Fluids* **36**, 076625.

HWANG, H.G. & LEE, J.H. 2018 Secondary flows in turbulent boundary layers over longitudinal surface roughness. *Phys. Rev. Fluids* **3**, 014608.

JIMENEZ, A., CRESPO, A., MIGOYA, E. & GARCIA, J. 2007 Advances in large-eddy simulation of a wind turbine wake. *J. Phys.: Conf. Ser.* **75**, 012041.

JOSHI, P. & ANDERSON, W. 2022 Surface layer response to heterogeneous tree canopy distributions: roughness regime regulates secondary flow polarity. *J. Fluid Mech.* **946**, A28.

KAMINARIS, I.K., BALARAS, E., SCHULTZ, M.P. & VOLINO, R.J. 2023 Secondary flows in turbulent boundary layers developing over truncated cone surfaces. *J. Fluid Mech.* **961**, A23.

KEVIN, K., MONTY, J.P., BAI, H.L., PATHIKONDA, G., NUGROHO, B., BARROS, J.M., CHRISTENSEN, K.T. & HUTCHINS, N. 2017 Cross-stream stereoscopic particle image velocimetry of a modified turbulent boundary layer over directional surface pattern. *J. Fluid Mech.* **813**, 412–435.

KIM, J. & MOIN, P. 1985 Application of a fractional-step method to incompressible Navier–Stokes equations. *J. Comput. Phys.* **59**, 308–323.

LI, Q., BOU-ZEID, E., ANDERSON, W., GRIMMOND, S. & HULTMARK, M. 2016 Quality and reliability of LES of convective scalar transfer at high Reynolds numbers. *Intl J. Heat Mass Transfer* **102**, 959–970.

LI, W. & GIOMETTO, M.G. 2023 Mean flow and turbulence in unsteady canopy layers. *J. Fluid Mech.* **974**, A33.

LI, W. & GIOMETTO, M.G. 2024 The structure of turbulence in unsteady flow over urban canopies. *J. Fluid Mech.* **985**, A5.

MARGAIRAZ, F., GIOMETTO, M.G., PARLANGE, M.B. & CALAF, M. 2018 Comparison of dealiasing schemes in large-eddy simulation of neutrally stratified atmospheric flows. *Geosci. Model Dev.* **11**, 4069–4084.

MEDJNOUN, T., VANDERWEL, C. & GANAPATHISUBRAMANI, B. 2020 Effects of heterogeneous surface geometry on secondary flows in turbulent boundary layers. *J. Fluid Mech.* **886**, A31.

MEILI, N. *et al.* 2020 An urban ecohydrological model to quantify the effect of vegetation on urban climate and hydrology (UT&C v1.0). *Geosci. Model Dev.* **13**, 335–362.

MEYERS, J. & MENEVEAU, C. 2013 Flow visualization using momentum and energy transport tubes and applications to turbulent flow in wind farms. *J. Fluid Mech.* **715**, 335–358.

MOMEN, M. & BOU-ZEID, E. 2017 Mean and turbulence dynamics in unsteady Ekman boundary layers. *J. Fluid Mech.* **816**, 209–242.

NIKURADSE, J. 1933 Laws of flow in rough pipes. *Tech. Memorandum* 1292. National Advisory Committee for Aeronautics.

OKE, T.R. 1982 The energetic basis of the urban heat island. *Q. J. R. Meteorol. Soc.* **108**, 1–24.

OKE, T.R., MILLS, G., CHRISTEN, A. & VOOGT, J.A. 2017 *Urban Climates*. Cambridge University Press.

ORSZAG, S.A. 1970 Analytical theories of turbulence. *J. Fluid Mech.* **41**, 363–386.

ORSZAG, S.A. & PAO, Y. 1975 Numerical computation of turbulent shear flows. *Adv. Geophys.* **18**, 225–236.

PERCIVAL, D.B. & MOFJELD, H.O. 1997 Analysis of subtidal coastal sea level fluctuations using wavelets. *J. Am. Stat. Assoc.* **92**, 868–880.

PRANDTL, L. 1925 Application of the magnus effect to wind propulsion of ships. *Tech. Memorandum* 367. National Advisory Committee for Aeronautics.

RAUPACH, M.R. & SHAW, R.H. 1982 Averaging procedures for flow within vegetation canopies. *Boundary-Layer Meteorol.* **22**, 79–90.

SALESKY, S.T., CHAMECKI, M. & BOU-ZEID, E. 2017 On the nature of the transition between roll and cellular organization in the convective boundary layer. *Boundary-Layer Meteorol.* **163**, 41–68.

SATHE, A.S. & GIOMETTO, M.G. 2024 Impact of the numerical domain on turbulent flow statistics: scalings and considerations for canopy flows. *J. Fluid Mech.* **979**, A36.

SCHLICHTING, H. 1937 Experimental investigation of the problem of surface roughness. *Tech. Memorandum* 1292. National Advisory Committee for Aeronautics.

SCHMID, M.F., LAWRENCE, G.A., PARLANGE, M.B. & GIOMETTO, M.G. 2019 Volume averaging for urban canopies. *Boundary-Layer Meteorol.* **173**, 349–372.

SCHULTZ, M.P. 2000 Turbulent boundary layers on surfaces covered with filamentous algae. *J. Fluids Engng* **122**, 357–363.

SCHULTZ, M.P. 2007 Effects of coating roughness and biofouling on ship resistance and powering. *Biofouling* **23**, 331–341.

SHARMA, V., CALAF, M., LEHNING, M. & PARLANGE, M.B. 2016 Time-adaptive wind turbine model for an LES framework. *Wind Energy* **19**, 939–952.

STROH, A., SCHÄFER, K., FROHNAPFEL, B. & FOROOGHI, P. 2020 Rearrangement of secondary flow over spanwise heterogeneous roughness. *J. Fluid Mech.* **885**, 1–12.

TIAN, G., CONAN, B. & CALMET, I. 2021 Turbulence-kinetic-energy budget in the urban-like boundary layer using large-eddy simulation. *Boundary-Layer Meteorol.* **178**, 201–223.

VANDERWEL, C. & GANAPATHISUBRAMANI, B. 2015 Effects of spanwise spacing on large-scale secondary flows in rough-wall turbulent boundary layers. *J. Fluid Mech.* **774**, R2.

VANDERWEL, C., STROH, A., KRIEGSEIS, J., FROHNAPFEL, B. & GANAPATHISUBRAMANI, B. 2019 The instantaneous structure of secondary flows in turbulent boundary layers. *J. Fluid Mech.* **862**, 845–870.

WANGSAWIJAYA, D.D., BAIDYA, R., CHUNG, D., MARUSIC, I. & HUTCHINS, N. 2020 The effect of spanwise wavelength of surface heterogeneity on turbulent secondary flows. *J. Fluid Mech.* **894**, A7.

WILLINGHAM, D., ANDERSON, W., CHRISTENSEN, K.T. & BARROS, J.M. 2014 Turbulent boundary layer flow over transverse aerodynamic roughness transitions: induced mixing and flow characterization. *Phys. Fluids* **26**, 025111.

WOMACK, K.M., VOLINO, R.J., MENEVEAU, C. & SCHULTZ, M.P. 2022 Turbulent boundary layer flow over regularly and irregularly arranged truncated cone surfaces. *J. Fluid Mech.* **933**, A38.

WU, Y. & CHRISTENSEN, K.T. 2006 Population trends of spanwise vortices in wall turbulence. *J. Fluid Mech.* **568**, 55–76.

WU, Y.T. & PORTÉ-AGEL, F. 2011 Large-eddy simulation of wind-turbine wakes: evaluation of turbine parametrisations. *Boundary-Layer Meteorol.* **138**, 345–366.

YANG, J. & ANDERSON, W. 2018 Numerical study of turbulent channel flow over surfaces with variable spanwise heterogeneities: topographically-driven secondary flows affect outer-layer similarity of turbulent length scales. *Flow Turbul. Combust.* **100**, 1–17.

YANG, X.I.A. 2016 On the mean flow behaviour in the presence of regional-scale surface roughness heterogeneity. *Boundary-Layer Meteorol.* **161**, 127–143.

YANG, X.I.A. & MENEVEAU, C. 2016 Recycling inflow method for simulations of spatially evolving turbulent boundary layers over rough surfaces. *J. Turbul.* **17**, 75–93.

ZHOU, J., ADRIAN, R.J., BALACHANDAR, S. & KENDALL, T.M. 1999 Mechanisms for generating coherent packets of hairpin vortices in channel flow. *J. Fluid Mech.* **387**, 353–396.